

Properties of galaxies at the faint end of the $H\alpha$ luminosity function at $z \sim 0.62$ \star

Carlos Gómez-Guijarro^{1,2}, Jesús Gallego¹, Víctor Villar^{1,3}, Lucía Rodríguez-Muñoz^{1,4},
Benjamin Clément⁵ and Jean-Gabriel Cuby⁶

¹ Departamento de Astrofísica y CC. de la Atmósfera, Facultad de CC. Físicas, Universidad Complutense de Madrid, Av. Complutense s/n, E-28040 Madrid, Spain
e-mail: cgguijarro@ucm.es

² Dark Cosmology Centre, Niels Bohr Institute, University of Copenhagen, Juliane Maries Vej 30, DK-2100 Copenhagen, Denmark

³ European Space Astronomy Centre, PO Box 78, E-28691 Villanueva de la Cañada, Madrid, Spain

⁴ Dipartimento di Fisica e Astronomia "G. Galilei", Università di Padova, Vicolo dell'Osservatorio 3, I-35122, Italy

⁵ CRAL, Observatoire de Lyon, Université Lyon 1, 9 Avenue Ch. André, F-69561 Saint Genis Laval Cedex, France

⁶ Aix Marseille Université, CNRS, LAM (Laboratoire d'Astrophysique de Marseille) UMR 7326, 13388, Marseille, France

Received 15 June 2015; accepted 14 April 2016

ABSTRACT

Context. Studies measuring the star formation rate density, luminosity function, and properties of star-forming galaxies are numerous. However, it exists a gap at $0.5 < z < 0.8$ in $H\alpha$ -based studies.

Aims. Our main goal is to study the properties of a sample of faint $H\alpha$ emitters at $z \sim 0.62$. We focus on their contribution to the faint end of the luminosity function and derived star formation rate density, characterising their morphologies and basic photometric and spectroscopic properties.

Methods. We use a narrow-band technique in the near-infrared, with a filter centred at $1.06 \mu\text{m}$. The data come from ultra-deep VLT/HAWK-I observations in the GOODS-S field with a total of 31.9h in the narrow-band filter. In addition to our survey, we mainly make use of ancillary data coming from the CANDELS and Rainbow Cosmological Surveys Database, from the 3D-HST for comparison, and also spectra from the literature. We perform a visual classification of the sample and study their morphologies from structural parameters available in CANDELS. In order to obtain the luminosity function, we apply a traditional V/V_{max} method and perform individual extinction corrections for each object to accurately trace the shape of the function.

Results. Our 28 $H\alpha$ -selected sample of faint star-forming galaxies reveals a robust faint-end slope of the luminosity function $\alpha = -1.46^{+0.16}_{-0.08}$. The derived star formation rate density at $z \sim 0.62$ is $\rho_{\text{SFR}} = 0.036^{+0.012}_{-0.008} M_{\odot} \text{ yr}^{-1} \text{ Mpc}^{-3}$. The sample is mainly composed of disks, but an important contribution of compact galaxies with Sérsic indexes $n \sim 2$ display the highest specific star formation rates.

Conclusions. The luminosity function at $z \sim 0.62$ from our ultra-deep data points towards a steeper α when an individual extinction correction for each object is applied. Compact galaxies are low-mass, low-luminosity, and starburst-dominated objects with a light profile in an intermediate stage from early to late types.

Key words. galaxies: fundamental parameters – galaxies: evolution – galaxies: star formation – galaxies: luminosity function, mass function

1. Introduction

The evolution of the luminosity function (LF) and the star formation rate (SFR) density across cosmic time has been an object of study over the last two decades. Since it was first addressed by the pioneering studies of Gallego et al. (1995); Lilly et al. (1996); and Madau et al. (1996), a wide view of the cosmic star formation history (SFH) has been revealed. The SFR density (SFRD) is now traced out to $z \sim 10$. The star formation activity grew from the formation of the first galaxies and reached a peak at $z \sim 2$. Then, the activity declined gradually until $z \sim 0$, when it reached values a factor of 10 smaller. Extensive compilations and reviews on this topic have been published over the years (Hopkins 2004; Hopkins & Beacom 2006; Behroozi et al. 2013; Madau & Dickinson 2014).

Diverse tracers have been used to infer SFRs (Kennicutt 1998; Kennicutt & Evans 2012). These indicators span a very broad wavelength range from gamma-ray/X-ray to radio. Among them, nebular emission lines such as $[\text{O II}]\lambda 3727$, $[\text{O III}]\lambda 5007$, $H\alpha$, and $H\beta$ have been frequently employed. The SFH based on all these tracers contribute to a comprehensive and consistent view on the evolution of star formation. However, there are discrepancies between the results obtained with different indicators at the same redshift, which are due to the intrinsic differences between galaxies selected with distinct criteria and between calibrations, the impact of dust extinction and metallicities, or observational biases. Particularly, the $H\alpha$ line has been widely used as an excellent method for measuring star formation (Gallego et al. 1995; Kennicutt 1998; Brinchmann et al. 2004; Kennicutt & Evans 2012). Because it is sensitive to stellar masses $\geq 15 M_{\odot}$ with ages $\sim 3\text{--}10$ Myr, $H\alpha$ is considered a direct tracer of the instantaneous SFR in a galaxy (Kennicutt & Evans 2012). The $H\alpha$ line is strong in the optical/near-infrared (NIR) range, it is less affected by dust extinction than other indicators like the ul-

\star Based on observations collected at the European Organisation for Astronomical Research in the Southern Hemisphere (ESO), Chile, Prog-Id 181.A-0485(A).

traviolet (UV) continuum, and it is not very sensitive to metallicity. Nevertheless, this tracer presents some drawbacks. It is currently restricted to redshifts $z \leq 2.23$. Over this value the line is redshifted beyond the wavelength limit of NIR spectrographs. In addition, the low efficiency in the transition from optical to NIR detectors makes the emission line virtually unreachable in the redshift range $0.5 < z < 0.8$. On the other hand, extinction-corrected $H\alpha$ SFRs are consistent with those derived from the total infrared (TIR) to far-ultraviolet (FUV) luminosity ratio (IRX) (Hao et al. 2011). The $H\alpha$ emission is tested as an exceptional way to measure star formation in the limit $z \sim 2$ (Oteo et al. 2015).

The existing literature in SFRD and LF measurements from $H\alpha$ is extensive. Gunawardhana et al. (2013) shows an exhaustive compilation of the SFRD results that use this tracer at different redshifts. Since then, new values of $H\alpha$ -based SFRDs have been published (Sobral et al. 2013; Drake et al. 2013; Gunawardhana et al. 2015; Sobral et al. 2015; Stroe & Sobral 2015).

Among these studies, two different techniques are employed: spectroscopic and narrow-band surveys. These techniques have advantages and drawbacks. Narrow-band surveys provide deep imaging in a narrow region in terms of redshift, selecting the candidates directly from the emission line under study. In addition, these filters are more effective in the detection of weak sources. On the other hand, there are disadvantages, such as dust obscuration, active galactic nuclei (AGN) contamination, insensitivity to low equivalent widths, and narrow redshift ranges that suffer from density variations due to different effects in the line of sight. Multislit spectroscopy can provide wide sky coverage and so it does not suffer from effects of cosmic variance or small statistics. Nevertheless, it is subject to slit signal losses and atmospheric effects that can limit the redshift access and can introduce undesirable selection effects. Slitless spectroscopy can avoid these concerns, but proper observations are time expensive.

In the optical regime, the work by Gallego et al. (1995, see also Pérez-González et al. 2003) first measured the local SFRD and LF using the Universidad Complutense de Madrid (UCM) Survey (Zamorano et al. 1994, 1996), an optical low-dispersion objective-prism survey for low-redshift emission-line galaxies (ELGs). Similar values were calculated at $z \sim 0$ from the SDSS (Brinchmann et al. 2004; Nakamura et al. 2004) and SINGG (Hanish et al. 2006) projects, and from local volume studies (James et al. 2008; Karachentsev & Kaisin 2010). Several authors extended local studies to redshifts $z < 0.3$ using optical spectroscopy (Tresse & Maddox 1998; Sullivan et al. 2000). The SHELS project analysed several slices in a redshift range up to $z < 0.4$ with a great number of spectra (Westra et al. 2010). Gunawardhana et al. (2013, 2015) have recently combined SDSS data with deeper optical spectroscopy from the GAMA survey to $z < 0.35$. Analogously, other authors obtained SFRDs with a narrow-band technique at $z \sim 0.24$ (Pascual et al. 2001; Fujita et al. 2003; Hippelein et al. 2003; Pascual 2005; Westra & Jones 2008; Shioya et al. 2008; Morioka et al. 2008; Westra et al. 2010) and $z \sim 0.4$ (Glazebrook et al. 2004; Pascual 2005). Other surveys collected large samples of objects with this technique within redshift slices up to $z < 0.4$ (Ly et al. 2007; Dale et al. 2010). Drake et al. (2013) has recently studied the cosmic SFH from $H\alpha$ in the redshift bins $z \sim 0.25, 0.4, 0.5$ with a total of 564 objects in the SXDS-UDS field.

In the NIR regime, object-by-object spectroscopic observations have provided important results in the ranges $0.79 < z < 1.1$ with 13 galaxies (Glazebrook et al. 1999), $0.5 < z < 1.1$ VLT/ISAAC observations of 30 galaxies (Tresse et al. 2002),

or $0.77 < z < 1$ spectra of 38 objects (Doherty et al. 2006). Several studies employed *HST*/NICMOS grism spectroscopy at $0.7 < z < 1.9$ (Yan et al. 1999; Hopkins et al. 2000; Shim et al. 2009). Narrow-band NIR works include redshift windows that are less affected by atmospheric features, such as $z \sim 0.84$ (Villar et al. 2008; Sobral et al. 2009; Ly et al. 2011), $z \sim 1.47$ (Sobral et al. 2012), and $z \sim 2.23$ (Moorwood et al. 2000; Geach et al. 2008; Hayes et al. 2010; Tadaki et al. 2011). The HiZELS survey has recently combined narrow-band data at common redshift windows $z \sim 0.4, 0.84, 1.47, 2.23$ and has obtained a view of the last 11 Gyr of evolution of star-forming galaxies (SFGs) by employing a homogeneously selected sample of $H\alpha$ emitters (Sobral et al. 2013). They have measured a constant value of the faint-end slope of the LF with redshift $\alpha \sim -1.6$ and a steady increase of the characteristic luminosity of the LF with redshift. The CF-HiZELS survey has surveyed $\sim 10 \text{ deg}^2$ deriving a sample of 3471 $H\alpha$ emitters at $z \sim 0.8$ (Sobral et al. 2015).

Our group measured the SFRD and LF locally (Gallego et al. 1995; Pérez-González et al. 2003) from a sample of $H\alpha$ emitters selected with an objective-prism survey, the UCM Survey (Zamorano et al. 1994, 1996). We then extended the study to $z \sim 0.24$ and $z \sim 0.4$ with an optical narrow-band technique (Pascual et al. 2001; Pascual 2005). More recently, we applied this technique in the NIR at $z \sim 0.84$ (Villar et al. 2008). In the mentioned redshift gap $0.5 < z < 0.8$ in $H\alpha$ -based studies, we only find a few objects in the lower limits of the NIR spectroscopic surveys indicated above. These limits are $z > 0.5$ (Tresse et al. 2002), $z > 0.77$ (Doherty et al. 2006), and $z > 0.79$ (Glazebrook et al. 1999). No narrow-band surveys cover this gap. In this work we use a narrow-band filter centred at $1.061 \mu\text{m}$ with the main goal of filling the $z \sim 0.6$ gap.

The layout of the paper is as follows. We describe the data and introduce the sample in Sect. 2. In Sect. 3 we characterise the sample properties: morphologies and stellar masses, followed by the calculation of line fluxes, luminosities, dust extinction, and a spectroscopic study. We obtain the $H\alpha$ -based LF for our sample at $z \sim 0.62$ in Sect. 4. We include a discussion in Sect. 5 and we summarise in Sect. 6.

Throughout this work we adopt a concordance cosmology $[\Omega_\Lambda, \Omega_M, h] = [0.7, 0.3, 0.7]$. Considering these parameters, the age of the universe at $z = 0.62$ is 7.63 Gyr, the luminosity distance is 3673.5 Mpc, and the scale $6.79 \text{ kpc}''$. An AB magnitude system is employed over the whole study (Oke 1974).

2. Data and sample selection

2.1. Narrow-band data: the VLT/HAWK-I survey

The main data used in this work correspond primarily to very deep NIR imaging observations with the HAWK-I instrument at the VLT. HAWK-I (Pirard et al. 2004; Casali et al. 2006; Kissler-Patig et al. 2008; Siebenmorgen et al. 2011) is a NIR (0.85–2.5 μm) wide-field imager installed at the Nasmyth A focus of ESO VLT UT4. The field of view is $7.5' \times 7.5'$. It is composed of four HAWAII 2RG detectors of 2048×2048 pixels. The pixel scale is $0.106''/\text{pix}$.

A narrow-band (NB) filter centred at $1.061 \mu\text{m}$ (NB1060) was employed. The data was obtained as part of an ESO large programme between September 2008 and April 2010 (project 181.A-0485(A), Clément et al. (2012)), that was devised to detect Ly α emitters (LAEs) at $z = 7.7$ in order to constrain the epoch of reionization. In this programme, four deep fields corresponding to blank and cluster regions were selected. Among them, the GOODS-S blank field was chosen because of the

great amount of multiwavelength data publicly available. For GOODS-S, the survey took a total integration time in the NB of 31.9 h and 3.3 h in the J band. Kochiashvili et al. (2015) has recently published a study focused on the main sequence of star-formation using ELGs at $z = 0.6-2$ within this large programme data. In our work, we make use of these deep GOODS-S images to extract a sample of H α emitters at $z \sim 0.62$. We then combine our NB photometry with ancillary data to study the properties of these systems.

2.2. Sample selection

We selected emission-line objects by comparing apparent fluxes in narrow-band and broad-band (BB) images. When an emission line falls within the NB filter, it produces an excess in this filter respect to the BB flux.

The same approach that was used to detect LAEs at $z = 7.7$ employing the NB1060 filter was found to be useful when selecting H α emission-line objects at $z \sim 0.62$. In particular, given the width of the NB filter, we cover a redshift range $0.6098 < z < 0.6263$. Because the NB1060 central wavelength $1.061 \mu\text{m}$ is placed in the Y band, we employed Y band as our BB filter. However, the transmittance of the Y -band filter starts to decrease at $1.06 \mu\text{m}$. In order to provide a proper account of the continuum flux, we interpolated its value with the contiguous J -band filter that was also available.

In detail, the selection process of the candidates was performed through a colour-magnitude diagram using the technique described in Pascual et al. (2007) and applied by our group in Villar et al. (2008). The criterion used was

$$(m_{\text{BB}} - m_{\text{NB}}) > \mu (m_{\text{BB}} - m_{\text{NB}}) + n_{\sigma} \sigma (m_{\text{BB}} - m_{\text{NB}}), \quad (1)$$

where m_{NB} and m_{BB} are the apparent magnitudes of the NB and BB filters, respectively, μ is an offset parameter that indicates the average deviation from the zero colour, σ is the standard deviation of the colour distribution, and n_{σ} is the level of significance. The values of μ and σ were calculated from the distribution of objects. These parameters are functions of the NB magnitude. Therefore, we obtained a curve that depends on the NB magnitude and the objects above it were selected as emission-line candidates. The fluxes in each band were measured using circular apertures of different sizes. The sample selection employed 9-10 apertures ranging from the PSF FWHM to 5 times this value.

We wanted to select emission-line objects at $z \sim 0.62$ avoiding non-emission line and redshift interlopers as much as possible. Thus, we needed to set the level of significance and the range of apertures that returned the best results.

We created several selection curves with n_{σ} from 1.5 to 3.0 in steps of 0.25. In each case, the defined sample was different. If the lowest n_{σ} was employed, the largest number of candidates was recovered, but many of them could be non-emission interlopers. On the other hand, if the level of significance grew, the returned sample was smaller, because the selection criterion became more restricted. We wanted to obtain the maximum number of candidates while maintaining the accuracy. Finally, we chose $n_{\sigma} = 2.5$. Villar et al. (2008) demonstrated that a good compromise between the number of objects and accuracy is obtained with this level of significance, a value also applied in other studies (Sobral et al. 2009).

In order to include as many emission-line emitters as possible, we needed to use several apertures. On the one hand, the smallest apertures detected small, low-luminosity emission-line objects and bright candidates with high nuclear star formation.

The fluxes for these candidates were less affected by sky emission. On the other hand, the largest apertures were better at selecting large, low surface-brightness objects with extended star formation. Large apertures for small emitters were not considered since the sky noise was high in these cases.

Once we selected the candidate emission-line emitters, we determined whether the object is a galaxy or a star. This segregation was carried out with the stellarity parameter from SExtractor. Objects with a stellarity parameter greater than 0.95 were considered stars.

We recovered a total raw sample of 46 candidate emission-line emitters. The lowest emission line equivalent width (EW) that we selected was $\sim 6 \text{ \AA}$. This selection result is in agreement with the sample of 58 candidates in Kochiashvili et al. (2015).

2.3. Incompleteness

The selection process described above suffers from selection effects, and recovers a different number of objects depending on the emission-line flux. In this kind of study this effect is commonly known as the incompleteness factor. The real number of emission-line emitters is higher than the number detected, and even higher for the faintest objects. In other words, the number of emission-line emitters is underestimated, and this effect is particularly important for the faintest sources. To take this effect into account, we used the results that our group obtained in Villar et al. (2008). In this work, a sample of simulated objects was introduced in the data, applying the same selection technique and measuring the fraction of objects recovered over the total as a function of the emission-line flux (see Villar et al. 2008, for details).

2.4. Photometric ancillary data

The CANDELS survey (Grogin et al. 2011; Koekemoer et al. 2011) is a powerful imaging survey of the distant universe carried out with the *HST*. It is designed to study galactic evolution from $z = 8$ to 1.5. To accomplish this objective it employs deep imaging of more than 250 000 galaxies with the WFC3/IR and ACS instruments.

For the present work we were interested in the advanced data products that the CANDELS project had released in the GOODS-S field. The CANDELS GOODS-S Multiwavelength catalogue (Guo et al. 2013) presents the multiwavelength photometry available in this field. It combines the newly obtained data from *HST*/WFC3 F105W, F125W, and F160W bands with previous ground-based public data. This catalogue is based on source detection in the WFC3 F160W mosaic, that includes the data from the CANDELS deep and wide programmes. The result is a catalogue of 34 930 sources in an area of 173 arcmin^2 . In addition to the WFC3 bands, this catalogue includes UV data (U band from CTIO/MOSAIC and VLT/VIMOS), optical (*HST*/ACS F435W, F606W, F775W, F814W and F850LP), and infrared (IR) (*HST*/WFC3 F098M, VLT/ISAAC K_s , VLT/HAWK-I K_s , and *Spitzer*/IRAC 3.6, 4.5, 5.8, $8.0 \mu\text{m}$). In addition to the photometric catalogue, the stellar masses have been recently published (Santini et al. 2015) and the structural parameters are available (van der Wel et al. 2012).

Furthermore, we used complementary mid-IR photometry in *Spitzer*/MIPS 24 and $70 \mu\text{m}$ ($30 \mu\text{Jy}$ and 1 mJy , 5σ) from Pérez-González et al. (2005, 2008b), and far-IR photometry from Pérez-González et al. (2010), the GOODS-*Herschel* survey (Elbaz et al. 2011), and the PEP survey (Magnelli et al. 2013) to

characterise the TIR luminosity of the galaxies. A description of the method used to derive consistent mid-to-far IR spectral energy distributions (SEDs) and rest-frame luminosities was presented in Pérez-González et al. (2008a) and Barro et al. (2011b). The mid- and far-IR fluxes and derived TIR luminosities for the sources in the CANDELS catalogue presented in Guo et al. (2013) are publicly available through the Rainbow Cosmological Surveys Database (Pérez-González et al. 2008a; Barro et al. 2011a,b)¹. The Rainbow Database also includes rest-frame near-ultraviolet (NUV) and FUV luminosities based on synthetic photometry (see Pérez-González et al. 2008a; Barro et al. 2011a,b, for details).

We used these sources to collect several measurements required for our study: astrometry, photometric redshifts (photo- z 's), stellar masses, structural parameters, photometry, rest-frame absolute magnitudes, synthetic TIR luminosity, and synthetic FUV and NUV magnitudes. We refer to TIR synthetic luminosity as that calculated via integration of SED from $8.0\ \mu\text{m}$ to $1000\ \mu\text{m}$. The FUV and NUV synthetic magnitudes are those obtained integrating the SED over the filter profiles.

We found counterparts in the CANDELS database for 42 objects out of the 46 candidate emission-line emitters in the original raw sample. They were confirmed as ELGs by the stellarity parameter, photo- z 's, and visual inspection of the postage stamps. The four objects with no CANDELS identification are those with reference numbers HAWKI0003148, HAWKI0003151, HAWKI0003361, and HAWKI0003606 in our original catalogue. If we try to visualise them in the CANDELS multicolour Interactive Display², we find that HAWKI0003148 and HAWKI0003151 are located beyond the images edges. HAWKI0003361 is either a star or it is contaminated by a neighbouring object. HAWKI0003606 does not appear on the CANDELS images, thus, it is an artefact or a very low-luminosity line emitter with no obvious continuum (apparent line flux from the NB image was $4.5 \times 10^{-18}\ \text{erg s}^{-1}\ \text{cm}^{-2}$). This last object is an extremely interesting candidate low-luminosity SFG with a very high EW. A more detailed analysis in the future will be needed to reveal its nature.

2.5. Spectroscopic ancillary data

In order to complete the information of the sample, we carried out a search of the spectroscopic data available in existing published studies. First, we performed a complete search in the ESO³, Centre de Données astronomiques de Strasbourg (CDS)⁴, and The VIMOS VLT Deep Survey (VVDS)⁵ archives, and also throughout the literature in the GOODS-S field.

Among the 46 objects selected in the raw sample, 13(28%) have a spectroscopic redshift (spec- z) determined. Seven of these targets have a FITS optical spectrum available in the archives mentioned above (Le Fèvre et al. 2004; Vanzella et al. 2008; Balestra et al. 2010). Five more galaxies have spectra measured from the ACES survey (Cooper et al. 2012). We analysed the FITS spectra and we remeasured the emission lines that we can identify. In Fig. 1 we show the collected spectra along with the identified emission lines and some basic data about the galaxies, including the spec- z 's.

¹ https://rainbowx.fis.ucm.es/Rainbow_navigator_public/

² http://archive.stsci.edu/prepds/candels/display_gs-tot_v1.0.html

³ <http://archive.eso.org/cms.html>

⁴ <http://vizier.u-strasbg.fr/viz-bin/VizieR>

⁵ <http://cesam.lam.fr/vvdsproject/>

In addition, we looked for additional spectroscopic data in the 3D-HST survey (Skelton et al. 2014), a NIR spectroscopic survey designed to study the physical processes that shape galaxies in the universe at $z > 1$. Although the instrumental set-up of this programme is very badly suited to observe emission-line emitters at $1.06\ \mu\text{m}$, its depth was able to provide spec- z 's for some objects in our sample. We found six counterparts for which we had already found a spec- z . Four of them show exactly the same value and the other two correspond to ancillary spectra with high quality flag, so we decided to maintain the values of the ground-based spectra and to discard the 3D-HST data. Moreover, 3D-HST provides a determination of the photo- z 's and stellar masses. Comparing them with the CANDELS data we did not find deviations out of the uncertainties except for two objects: CANDELS 12039 = 3D-HST 23397 and CANDELS 18444 = 3D-HST 3408. We decided to keep the CANDELS values except in the two discrepant cases for which the 3D-HST values appeared more suitable to the colours and morphologies these galaxies show in their postage stamps. Actually, these two systems are characterised by blue colours and low masses, properties that make the photo- z estimation more difficult. In particular, they show none or a small 4000 Å break feature and the photometry beyond the F160W band is close to detection limits. It is worth looking at grism data for this kind of objects with signs of emission lines with high EW.

2.6. Photometric redshifts

One of the products we took from CANDELS were the photo- z 's. We accessed them through the stellar masses catalogue (Santini et al. 2015). The final CANDELS photo- z catalogue in the GOODS-S field is not available yet, although a preliminary study on photo- z estimation methods has been published (Dahlen et al. 2013). This work consists of a comparison between several photo- z codes using a control sample of accurate spec- z 's. In practice, the authors test the dependence of photo- z 's on code and SED templates. They conclude that there is no particular code or SED template library that provides a better determination of the photo- z 's. Finally, they combine the results and obtain lower photo- z scatter. Our aim is to use the photo- z 's as a way to discriminate between $H\alpha$ ELGs or interlopers at other redshifts when we lack spec- z 's (see Sect. 2.7).

For our sample, we compared the CANDELS photo- z 's with the available spec- z 's from the literature. Twelve out of the 13 objects with spec- z are classified at $z \sim 0.6$ by the photo- z and the spec- z confirms them as $H\alpha$ emitters at $z \sim 0.62$. The object CANDELS 16483 has photo- $z = 1.91$ and spec- $z = 1.17$, being confirmed as an $H\beta$ emitter at $z \sim 1.17$. This means that the accuracy of the photo- z 's is good enough for our purpose of distinguishing between $H\alpha$ emitters and interlopers at other redshifts.

2.7. $H\alpha$ emitters and interlopers at other redshifts

With the collected spec- z 's and the CANDELS photo- z 's, we estimated the number of different ELGs among the 42 objects with a CANDELS counterpart. Photo- z 's suggest that the number of $H\alpha$ emitters at $z \sim 0.62$ are 28(67%). Among them 12(29%) are spectroscopically confirmed. In addition, one is a (2%) $[S\ III]\lambda 9069$ emitter at $z \sim 0.2$ (CANDELS 17704), eight (19%) $H\beta$ or $[O\ III]\lambda\lambda 4959,5007$ at $z \sim 1.1$, and three (7%) $[O\ II]\lambda 3727$ at $z \sim 1.8$ (CANDELS 14122, 17075, and 17686). One of the $H\beta$ emitters (CANDELS 16483) is spectroscopically

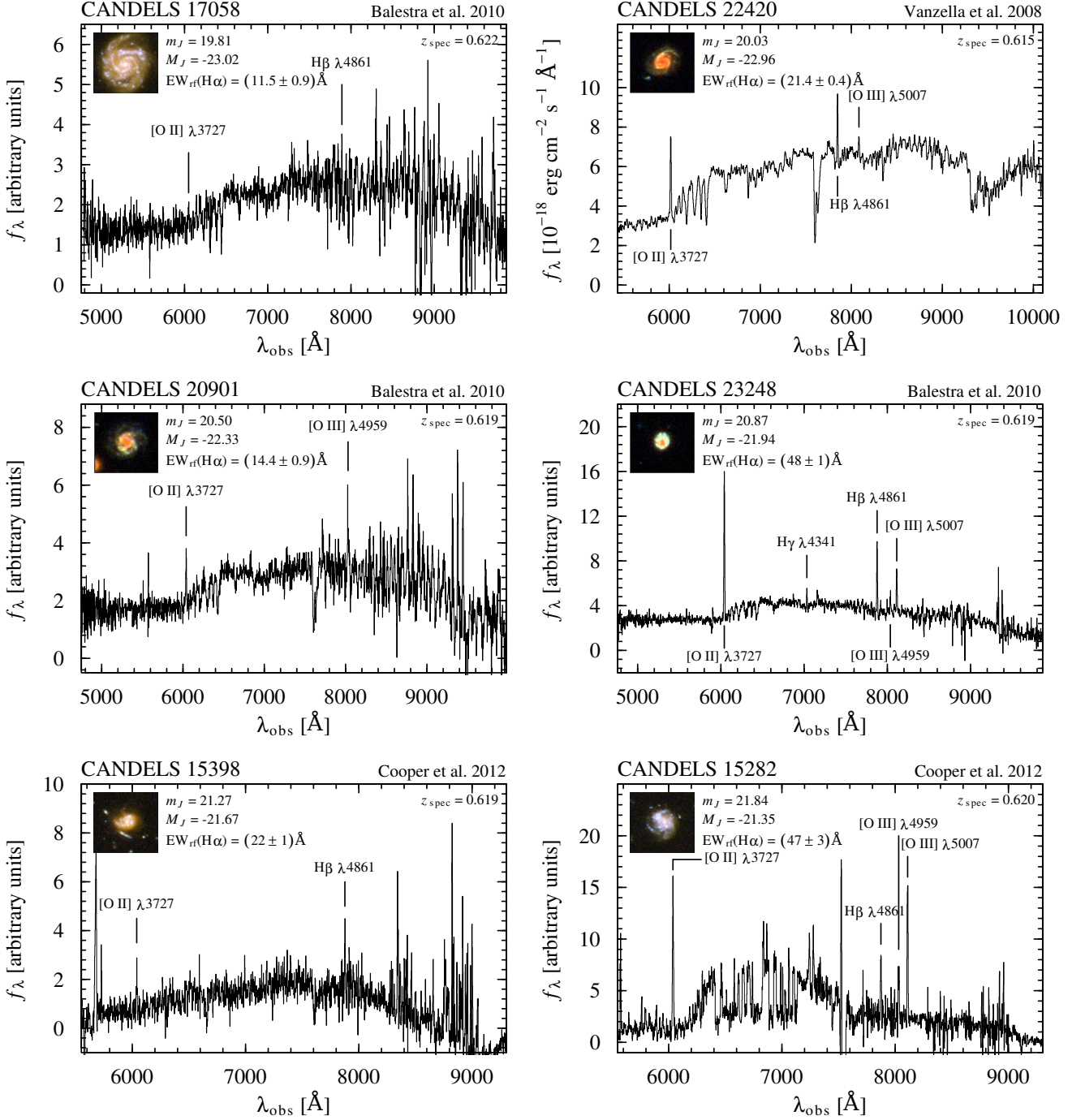


Fig. 1. Spectra collected from the literature. Among the 46 objects selected in the raw sample, 12(26%) have a FITS optical spectrum available. Each spectrum shows the CANDELS ID and the reference on top; an RGB image built using ACS b , v , and z bands with north up, east left, and a size of $5'' \times 5''$; the spec- z taken from the reference; observed J -band apparent magnitude; rest-frame J -band absolute magnitude; $H\alpha$ rest-frame EW (observed EW is $1+z$ times the rest-frame value); and the identification of the emission lines that we can measure.

confirmed and it appears at the ACS images as a blue compact object (see Fig. 3). Finally, two objects (5%) have photometric redshift $z > 2.5$ (CANDELS 11513 and 18444). We summarise this information in Table 1.

In Fig. 2 we present a rest-frame $U - V$ versus $V - J$ diagram (i.e. the UVJ diagram). This diagram is used in many studies to discriminate between SFGs and quiescent galaxies (Williams et al. 2009; Patel et al. 2012). We took the rest-frame absolute magnitudes from the CANDELS stellar masses catalogue (Santini et al. 2015). The catalogue does not provide uncertainties,

so we assumed a 0.2 mag photometric uncertainty in the absolute magnitudes, although in SED-fitting derived magnitudes of this kind, the main source for errors is the model assumption. With this diagram, we checked that our selection of $H\alpha$ emitters at $z \sim 0.62$ lie in the SFG region within the uncertainties. We split the sample into three mass bins: $\log(M/M_\odot) < 8.5$, $8.5 < \log(M/M_\odot) < 9.5$, and $\log(M/M_\odot) > 9.5$. Low-mass galaxies have lower $U - V$ and $V - J$ colours. In contrast, high-mass systems have higher $U - V$ and $V - J$ colours. These colours are an indication that low-mass galaxies have an impor-

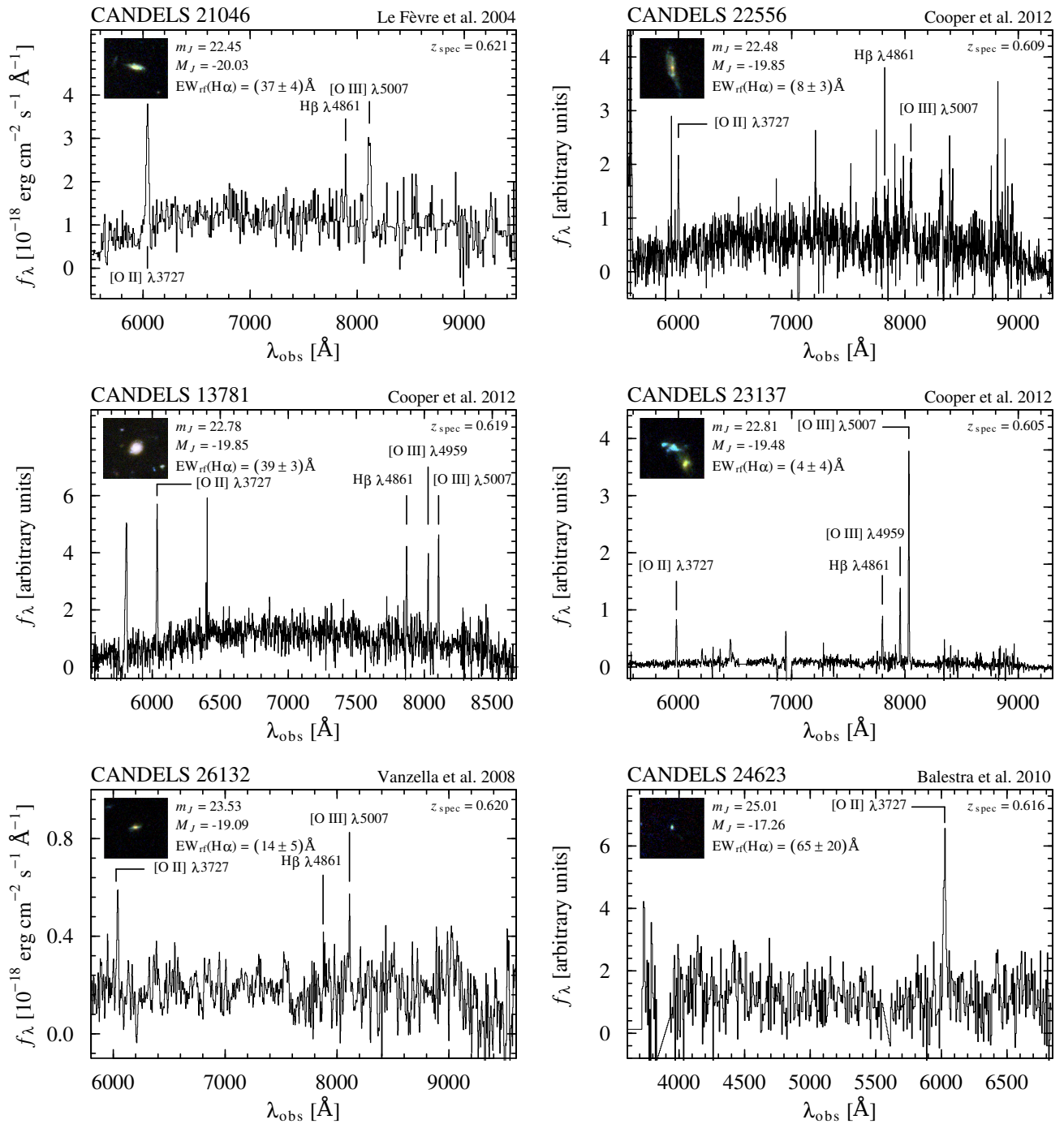


Fig. 1. continued.

tant young stellar population that dominates the emission and high-mass are more dominated by an older stellar population.

2.8. AGN contribution

We checked the sample by searching for an AGN contribution. If we detected any AGN we rejected them in the final sample as we only wanted to study the contribution of SFGs. We performed a search in the CDF-S field through the 4Ms source catalogues (Xue et al. 2011), the deepest *Chandra* survey to date. We only found X-ray detection for the object CANDELS 20901, with absorption-corrected rest-frame 0.5–8 keV luminos-

ity of $3.8 \times 10^{41} \text{ erg s}^{-1}$. This object is not classified as an AGN by the 4Ms catalogues. Furthermore, the spectroscopic data available does not indicate an AGN contribution in this galaxy (see Fig. 1 and Sec. 3.5). Consequently, we have no apparent AGN contribution in our sample of ELGs.

3. Properties of H α star-forming galaxies

3.1. Morphologies

We generated RGB postage stamps of the objects in our sample from the Rainbow Database. We used three filters of *HST*/ACS. The colour blue was assigned to the F435W band, green to the

Table 1. Summary of numbers and percentages of $H\alpha$ emitters and interlopers at other redshifts within the 42 galaxies with CANDELS counterparts.

Line ^a	z	Number	Percentage
$H\alpha$	~ 0.62	28(12)	67%(19%)
[S III]	~ 0.2	1	2%
$H\beta$	~ 1.17	8(1)	19%(2%)
[O II]	~ 1.8	3	7%
(...)	> 2.5	2	5%

Notes. The numbers and percentages of the spectroscopically confirmed objects are in parentheses.

^(a) Simplified notation: [S III] λ 9069 emitters at $z \sim 0.2$ are indicated as [S III]; $H\beta$ or [O II] λ 4959,5007 at $z \sim 1.1$ as $H\beta$; [O II] λ 3727 at $z \sim 1.8$ as [O II].

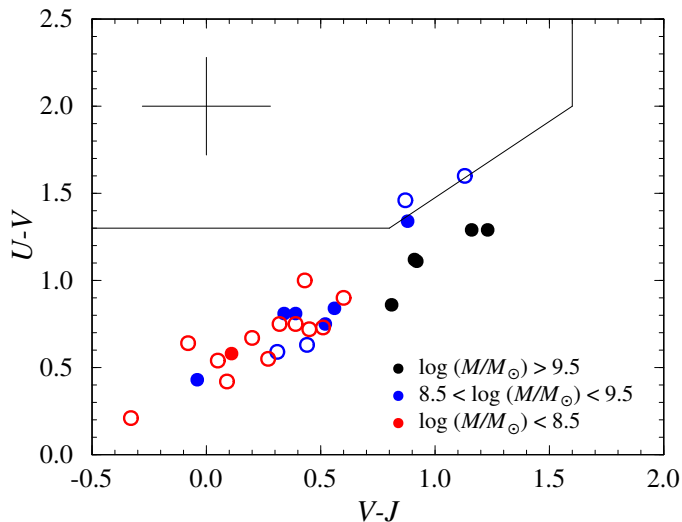


Fig. 2. UVJ diagram, rest-frame $U - V$ vs. $V - J$ for our sample of 28 $H\alpha$ SFGs at $z \sim 0.62$. The black edge boundary from Williams et al. (2009) separates quiescent galaxies (top left) from SFGs. The sample is divided into three mass categories as explained in the legend. Filled circles indicate those galaxies with available spectra. Average error bars are in the upper left corner.

F606W band, and red to the F850W band. In this configuration, we observe the rest-frame spectral range of NUV, B , and V bands for an object at $z \sim 0.62$. Therefore, we show regions associated with star formation and young populations in blue and green and a more evolved stellar population in red. In addition, we searched in the II/258 Hubble Ultra Deep Field Catalog (UDF) (Beckwith 2005) and found 11 results. We used the UDF SkyWalker⁶ tool to create images with a greater exposure time and quality than the ones we obtained from the Rainbow Database for these 11 objects. The filters used in this case are similar: ACS F435W, F606W, F775W, and F850LP. We present the final RGB postage stamps of the 42 objects with CANDELS counterparts in Fig. 3. Thirty-one of them come from the Rainbow Database and 11 from the UDF Skywalker.

We were able to develop a visual morphological classification for our objects. We used the z band ACS image in the GOODS-S field. We based it on the CANDELS morphological classification in Kartaltepe et al. (2015). In this work, the authors classify the objects in five main categories: ‘Disk’, ‘Spheroid’,

‘Irregular’, ‘Compact’, and ‘Unclassifiable’. They add mixed classes, but we decided to maintain only the main categories.

The Disk category includes objects with a disk structure. Among the Disk objects, we classify those that show a clear spiral structure as ‘Spiral’ and those that do not as Disk. Spheroidal galaxies appear concentrated and round or ellipsoidal. Irregular objects includes galaxies that do not fall into the other categories because they show irregular/peculiar structures. Strongly disturbed objects are included here, but also those disks or spheroids with slightly disturbed morphologies. Compact objects are clear point sources, unresolved compact galaxies, or are too small to show internal features. A small but clearly resolved spheroidal galaxy is classified as a Spheroid. Unclassifiable objects cannot be placed in another main category because there is problem in the image or because they are too faint to show any structure.

We also include the interaction flags ‘Merger’, ‘Interaction’, and ‘Close Neighbour’. The Merger flag is used to signal objects that show tidal and structure features such as tails or loops. All these objects are classified as Irregular in the main category scheme. The Interaction flag refers to primary objects that appear to be interacting with a companion galaxy. Interactions show tidal features. To be assigned this flag instead of Merger, two galaxies must be visible. Close Neighbour refers to galaxies with a close visible companion in the field of view of the postage stamp. No evidence of tidal interaction or disturbed morphology is apparent.

In Table 2 we show the results of this visual morphological classification for two groups: Total, which comprises the 42 objects with CANDELS counterparts, and $H\alpha$, which comprises the 28 $H\alpha$ emitters mentioned in Sect. 2.7. We see that the majority of our objects are Disk or Irregular in the Total sample and Disk in the $H\alpha$ sample. In terms of interactions, 79%(79%) have a Close Neighbour, 10%(11%) show signatures of Interaction, 5%(4%) are Merger, and 6%(6%) do not show any interactions features in the Total($H\alpha$) sample. We do not find any significant differences between the Total and $H\alpha$ samples in terms of interactions.

It is important to comment on the uncertainties of the morphological classification. It can be difficult to classify some of the objects as we are mainly dealing with small and faint sources. Some irregular features are hard to see or could remain undetected because of their intrinsic low surface-brightness. This effect could cause a bias in the Irregular category towards Disk.

In order to perform a more complete morphological characterisation of our sample, we studied the structural parameters. In Fig. 4 we show, for the 42 objects with CANDELS counterparts, the rest-frame B -band absolute magnitude versus the effective radius taken from the CANDELS stellar masses (Santini et al. 2015) and photometric catalogues (Guo et al. 2013), respectively. The catalogues do not provide uncertainties for these parameters. We assumed a 0.2 mag photometric uncertainty in the absolute magnitude as is indicated in Sect. 2.7. In the case of the effective radius, we assumed 1 pix uncertainty. We refer to Phillips et al. (1997) for a similar diagram in which the authors studied the location of a sample of compact galaxies in the diagram in comparison with other local types. From a quick look at our plot, we note a tendency that Spheroid and Compact galaxies are fainter and more compact, and Spiral galaxies are brighter and larger (i.e. less compact). Moreover, the Unclassifiable CANDELS 17503 and 31370 are the two faintest objects, as is expected from their morphological category.

In Fig. 4 we identified similarities between various visual categories. Different morphological classifications overlap in the

⁶ <http://www.aip.de/groups/galaxies/sw/udf/swudfV1.0.html>

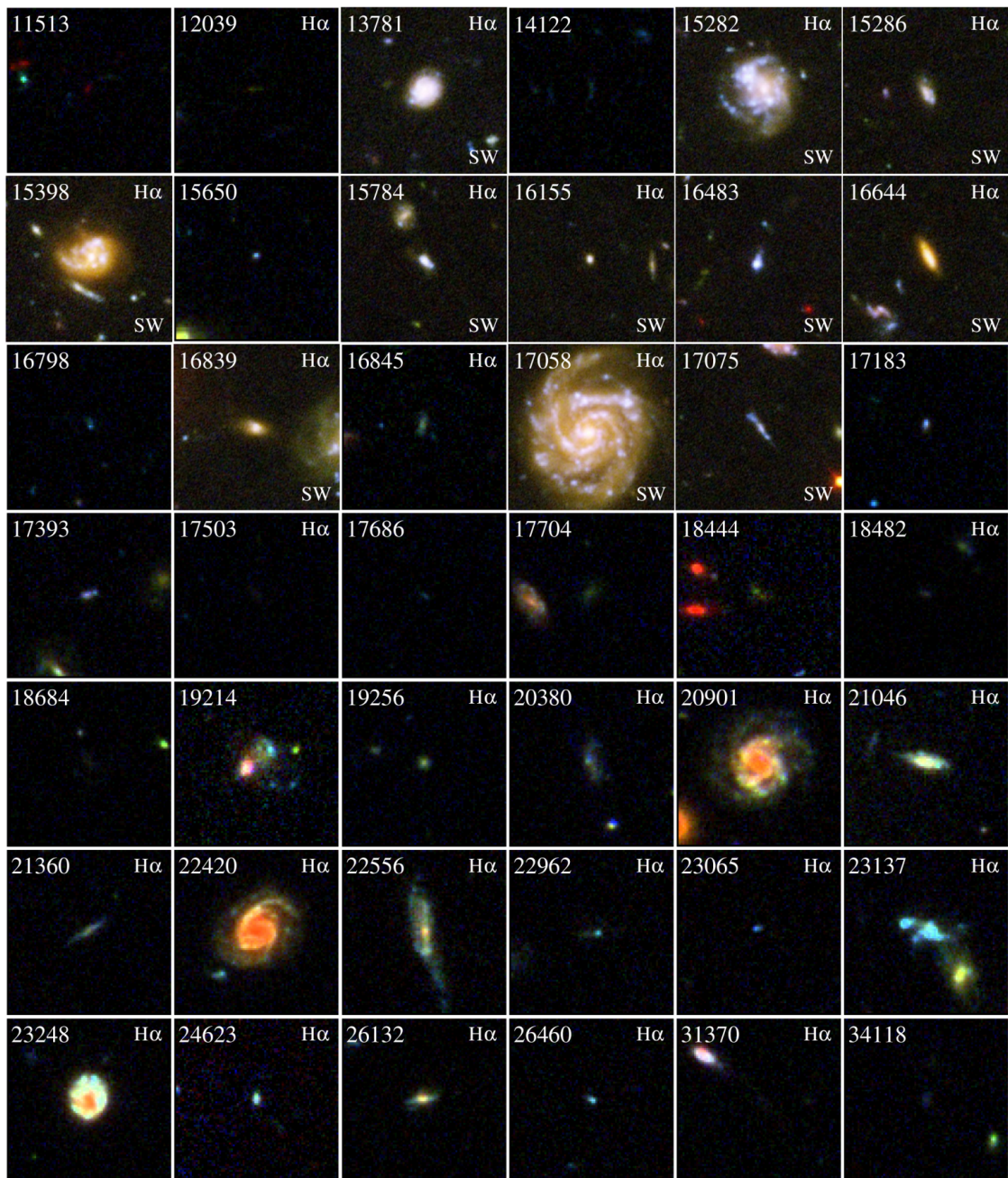


Fig. 3. RGB postage stamps of the 42 objects in our raw sample with CANDELS counterparts. North is up, east is to the left, and the images have a size of $5'' \times 5''$. The CANDELS ID is in the upper left corner. Those classified as $H\alpha$ emitters show this label in the upper right corner. Those images built with UDF Skywalker show the label SW in the bottom right corner.

Table 2. Visual morphological classification.

Sample	Spiral	Disk	Spheroid	Compact	Irregular	Unclassifiable
Total ^a	6(14%)	15(36%)	4(9%)	2(5%)	13(31%)	2(5%)
$H\alpha$ ^b	6(21%)	13(46%)	3(11%)	1(4%)	3(11%)	2(7%)

Notes. ^(a) Numbers(percentages) of the Total sample of the 42 objects with CANDELS counterparts. ^(b) Numbers(percentages) of the objects classified as $H\alpha$ emitters.

same region of the plot. Compact and Spheroid objects tend towards low sizes and luminosities, whereas the Spiral category, where some of the Disk galaxies are located as well, is biased to large and bright objects. In order to better constrain this, we studied other available structural parameters for our sample in the

CANDELS structural parameters catalogue (van der Wel et al. 2012). From this catalogue, we selected only the counterparts with a good GALFIT flag (flag = 0). In Fig. 5 we show several of these parameters along with the Sérsic index, a parameter that allows us to establish a continuous way to morphologically

classify the galaxies. We were able to see the similarities and differences in terms of blue luminosities (M_B), compactness (effective radius, r_e), and roundness (axis ratio, b/a) with morphology. In this case, we assumed a 0.2 mag photometric uncertainty in the absolute magnitude with the values taken from Santini et al. (2015) shown in Fig. 4. The uncertainties in the structural parameters were taken from van der Wel et al. (2012). There is a clear contrast between the galaxies CANDELS 15784, 16155, and 19256, which have Sérsic indexes of $n \sim 2-3$, and the rest, which have $n < 1.5$. Spirals show the highest luminosities, the largest radii and axis ratios close to one. We note that the number of objects in Fig. 4 is greater than in Fig. 5 because in the latter we only consider those sources with reliable parameters in the van der Wel et al. (2012) catalogue.

Taking into account all these structural parameters, we re-distributed the galaxies in the different morphological categories in order to look for an even simpler approach. We looked at the structural similarities rather than the differences in the detailed features that we considered in the visual morphological classification. We can say that we had no reason to distinguish between Spheroid and Compact objects for our sample. They are compact and faint single starburst candidates that dominate the entire galaxy. The Sérsic index would be $n \sim 2-3$ for galaxies of this kind. The Irregular CANDELS 15784 just presents a difference in terms of the axis ratio ($b/a = 0.34 \pm 0.02$), compared to Compact(Spheroid) morphologies ($b/a > 0.6$). It could be the star formation or its companion that is disrupting its shape. The Irregular CANDELS 26460 could be a pre- or post-stage Compact(Spheroid) class, as the difference with this category in terms of the Sérsic index ($n = 0.65 \pm 0.26$) could be explained if the light is more disperse owing to a nuclear starburst that has not completely started or a disruption once the star formation has finished. The last Irregular CANDELS 23137 is a Merger with structural properties more related to Disk morphology, ($M_B = -19.42$, $r_e = 0.52$). In the case of Spiral and Disk classes, we only see a difference in terms of luminosities and sizes; the Sérsic indexes are $n < 1.5$ in every case. The Spiral class is linked to observational effects. It is biased to face-on, brighter, and larger objects. It is easier to distinguish features in brighter and larger disks and we cannot distinguish spiral characteristics in edge-on objects. These galaxies tend to have larger Sérsic indexes. Within the Disk category we find a continuous distinction between the smallest disks closer to compact objects, in terms of luminosities and compactness, and larger disks related with spiral features. We should include all disks in the same Disk category regardless of their spiral structures since all these features are associated with biased interpretations rather than a difference in nature.

3.2. Stellar masses

The stellar masses are another product that we took from CANDELS in the GOODS-S field (Santini et al. 2015). The authors use the same data to compute masses through ten different codes and then they combine the results. We compared the CANDELS stellar masses with those released by 3D-HST (Skilton et al. 2014). We measured an offset median = -0.057 with a $rms = 0.26$ once we eliminated the outliers CANDELS 12039 = 3D-HST 23397 and CANDELS 18444 = 3D-HST 3408. The offset is defined as $\log(M_{\text{median}}^{\text{CANDELS}}/M^{\text{3D-HST}})$. Our offset perfectly matches the median = -0.058 ± 0.003 measured in Santini et al. (2015). The authors of the CANDELS stellar mass catalogue argue that, because the comparison is satisfying at a first order, the differences between the two catalogues are due to different sys-

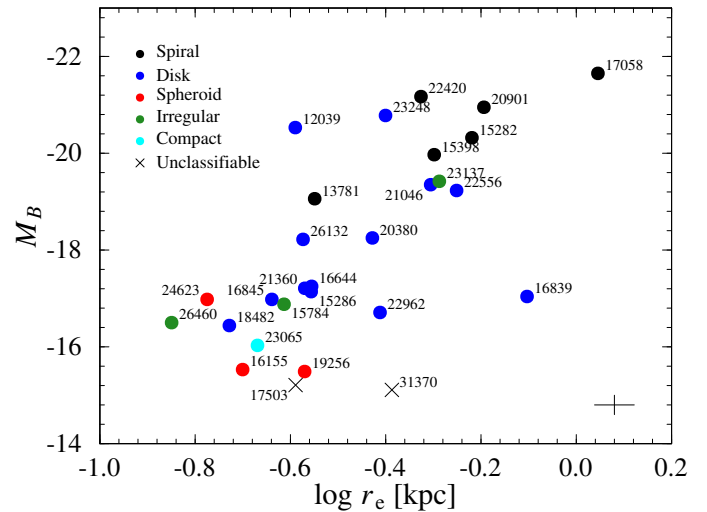


Fig. 4. Rest-frame B -band absolute magnitude vs. effective radius measured in the F160W band for the 42 objects in our sample with CANDELS counterparts. We show the morphological classification of each object as it is indicated in the legend. Error bars are indicated in the bottom right corner.

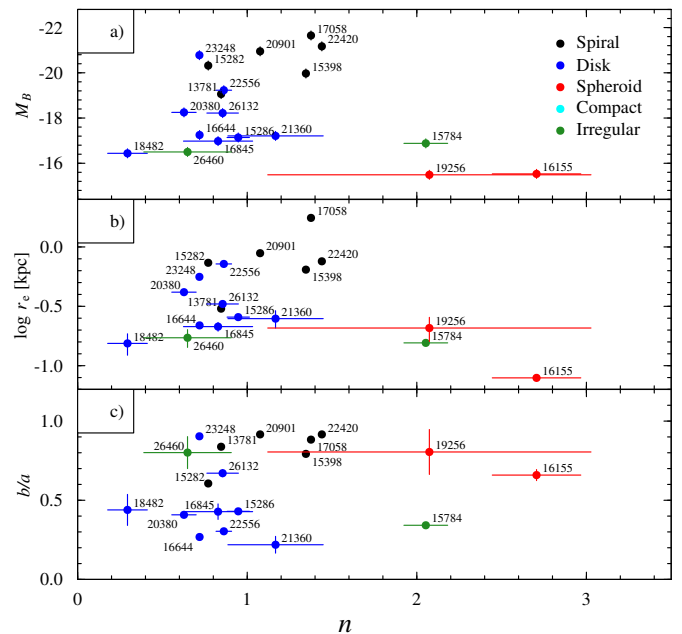


Fig. 5. Structural parameters from van der Wel et al. (2012) measured in the F105W band. a) Rest-frame B -band absolute magnitude vs. Sérsic index. b) Effective radius vs. Sérsic index. c) Axis ratio vs. Sérsic index. We show the morphological classification with the colour code indicated in the legend.

tematics in the SED fitting. The 3D-HST masses come from a single fit, but CANDELS values follow a median approach that deal better with the systematics because of the model assumptions. For the outliers we decided to substitute the CANDELS masses for the 3D-HST values as we indicated in Sect. 2.5. The 3D-HST catalogue does not provide uncertainties in the stellar masses, and so we assumed a typical 20%. In Fig. 6 we present a histogram of the distribution of stellar masses in our 42 galaxies sample with CANDELS counterpart. In blue we indicate the 28 objects confirmed as $H\alpha$ emitters.

3.3. Line flux and line luminosity estimation

In order to obtain the emission-line fluxes from the NB, we followed the Pascual et al. (2007) approach as described and applied in Villar et al. (2008). In a recent study by Vilella-Rojo et al. (2015), the authors find that $H\alpha + [N II]$ fluxes obtained with the combination of two filters are underestimated by 28% compared to the fluxes derived via SED fitting. It is important to take this into account when comparing fluxes calculated with different techniques.

Emission-line fluxes are computed using

$$f_l = \Delta_{NB} (f_{NB} - f_{BB}) \frac{1}{1 - \epsilon}, \quad (2)$$

where f_{NB} and f_{BB} are the total fluxes in the NB and BB filters, f_l is the line flux including the contribution of $[N II]\lambda\lambda 6548, 6584$, Δ_{NB} is the NB filter width, and ϵ is the ratio of NB and BB widths.

To calculate the integrated emission-line flux of each galaxy, we used several apertures because the galaxies show a variety of sizes and shapes. The flux grows with the aperture diameter until the limit of the emission region is reached. Nitrogen contamination in the NB fluxes was removed following the indications in Villar et al. (2008), where the authors study the trend between $\log(I([N II]\lambda 6584)/I(H\alpha))$ and $\log(EW(H\alpha + [N II]\lambda 6584))$ in SDSS galaxies to get a relation to estimate $[N II]$ contribution to the emission-line flux in the NB images for each source. In Fig. 6 we can see the flux distribution of the 46 candidates primarily selected. This value grows as we move to fainter magnitudes until the detection limit is reached.

Once the emission-line flux is calculated, the emission-line luminosity is immediate using

$$L = 4\pi d_l^2(z) f_l, \quad (3)$$

where $d_l(z)$ is the distance luminosity. We used the cosmological library *Milia* (Pascual 2015)⁷ to compute it. We employed the spec- z 's if available and the value $z = 0.62$ otherwise.

3.4. Reddening correction

The line fluxes and luminosities that we calculated in Sect. 3.3 are observed values, and so are uncorrected for dust extinction. We needed to develop a strategy to take into account the various sources of attenuation: the intrinsic extinction from the studied galaxy and the extinction from our own Galaxy. We followed the method employed by Villar et al. (2008). The extinction-corrected fluxes and luminosities are then

$$\log f_{l,cor} = \log f_l + 0.4 (A(\lambda_{rf}) + a(\lambda_z)), \quad (4)$$

$$L = 4\pi d_l^2(z) f_{l,cor}, \quad (5)$$

where $A(\lambda_{rf})$ is the intrinsic extinction of the studied galaxy at the rest-frame wavelength and $a(\lambda_z)$ is the Galactic attenuation at the observed frame field.

For $a(\lambda_z)$ we took a constant value of 0.006 mag as measured in UKIRT J band ($1.25 \mu m$) for the coordinates of the GOODS-S field (Schlafly & Finkbeiner 2011). It is a completely negligible value compared with the intrinsic extinction.

On the other hand, it is known that dust absorbs an amount of the star emission. This dust emits it again in the IR. Therefore,

⁷ <http://guaix.fis.ucm.es/projects/milia>

a good approach for calculating the intrinsic extinction of the studied galaxy is to study the ratio between dust and FUV fluxes (F_{dust}/F_{FUV}), the IRX ratio. This value is related to the FUV extinction $A(FUV)$ (Buat et al. 2005):

$$A(FUV) = -0.0333y^3 + 0.3522y^2 + 1.1960y + 0.4967, \quad (6)$$

where $y = \log\left(\frac{F_{dust}}{F_{FUV}}\right)$.

We obtained F_{dust} from the TIR luminosity synthetically calculated and F_{FUV} from synthetic FUV magnitude. Both of these values were taken from the Rainbow Database, as is indicated in Sect. 2.4. Then, we obtained the $H\alpha$ extinction ($A(H\alpha)$) with the $A(FUV)$ value applying a Calzetti extinction law (Calzetti et al. 2000):

$$A(H\alpha) = A(FUV) \frac{k_{H\alpha}}{k_{FUV}}, \quad (7)$$

where $k_{H\alpha} = 2.659 \left(-1.857 + \frac{1.040}{\lambda_{H\alpha}}\right) + R'_V$,

$k_{FUV} = 2.659 \left(-2.156 + \frac{1.509}{\lambda_{FUV}} - \frac{0.198}{\lambda_{FUV}^2} + \frac{0.011}{\lambda_{FUV}^3}\right) + R'_V$

and $R'_V = 4.05$.

For CANDELS 15282 we got a value $A(H\alpha) < 0$, thus, we assumed $A(H\alpha) = 0$. In the case of CANDELS 12039 the synthetic TIR luminosity was not available and we calculated the extinction employing FUV and NUV synthetic magnitudes from the Rainbow Database. The FUV – NUV colour is related to the IRX ratio (Muñoz-Mateos et al. 2009):

$$\frac{L_{TIR}}{L_{FUV}} = 10^{0.30+1.15(FUV-NUV)} - 1.64. \quad (8)$$

Once we have the IRX ratio from Eq. 8, we can substitute it in Eq. 6 and apply a Calzetti law (Eq. 7) to obtain the extinction for this object.

In Fig. 6 we show the distribution of the sample in terms of stellar masses, rest-frame B -band absolute magnitude and $B - V$ colour, which we took from the CANDELS stellar masses catalogue (Santini et al. 2015). We also show the $H\alpha$ line flux, $H\alpha$ rest-frame EW, and $H\alpha$ extinction that we calculated in this section. We separate the contribution of the 28 confirmed $H\alpha$ emitters in blue. We cannot see any significant difference between the $H\alpha$ emitters properties and the interlopers at other redshift that form the whole sample. We highlight the presence of very low line fluxes, luminosities, and stellar masses within the sample. In Table 3, at the end of the document, we gather the complete information and calculations of the sample.

3.5. Spectroscopy

As was described in Sect. 2.5, we collected the 12 spectra shown in Fig. 1. In this section, we present the outcome obtained through the spectra analysis. Making use of the software IRAF and the task *splot*, we measured the emission lines that we identified in each spectrum. We performed ten measurements of each line, taking the average value of them with the standard deviation as the uncertainty. The spectroscopic properties of ELGs are generally characterised using line-ratio diagnostic diagrams (Baldwin et al. 1981; Veilleux & Osterbrock 1987). We focus the analysis on two diagrams: excitation versus luminosity and rest-frame EW($[O III]$) versus luminosity. These diagrams are common in studies of this kind (Gallego et al. 1997; Guzmán et al. 1997).

In Fig. 7 we present the $[O III]\lambda 5007/H\beta$ versus M_B diagram. The ratio $[O III]$ to $H\beta$ is an indicator of the excitation of the

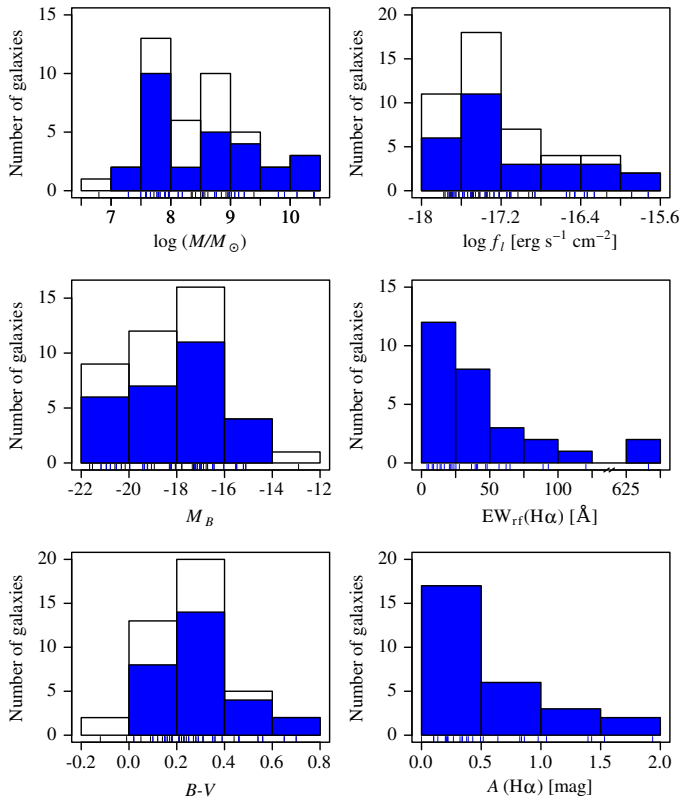


Fig. 6. Histograms of several magnitudes. In white, the 42 galaxies with CANDELS counterparts and in blue the sample of 28 $H\alpha$ SFGs. *Top left panel:* histogram of stellar masses. *Middle left panel:* histogram of rest-frame B -band absolute magnitude. *Bottom left panel:* histogram of $B - V$ colour. *Top right panel:* histogram of line fluxes. In this case, we show in white the raw sample of 46 candidates and the 28 $H\alpha$ objects overlapped in blue. *Middle right panel:* histogram of $H\alpha$ rest-frame EW for the 28 $H\alpha$ emitters. *Bottom right panel:* histogram of $H\alpha$ extinction for the $H\alpha$ SFGs.

ionized gas. As noted in Guzmán et al. (1997), the galaxies in this diagram are distributed following a sequence analogous to the $H\text{II}$ sequence in the $[\text{O III}]/\text{H}\beta$ versus $[\text{N II}]/\text{H}\alpha$ diagram (Veilleux & Osterbrock 1987). This sequence indicates a variation in the metallicity of the gas (Dopita & Evans 1986) through the $[\text{O III}]/[\text{N II}]$ ratio (Pettini & Pagel 2004; Marino et al. 2013). Along the sequence, the metallicity grows with luminosity (i.e. lower $[\text{O III}]/[\text{N II}]$ ratio). We separate the galaxies into three mass bins: $\log(M/M_\odot) < 8.5$, $8.5 < \log(M/M_\odot) < 9.5$, and $\log(M/M_\odot) > 9.5$. In this case none of the objects is in the first bin. We can see a wide range in excitation and metallicity and a clear difference in terms of mass. The intermediate-mass galaxies show higher excitation (i.e. lower metallicity) than the high-mass galaxies. We include references to SDSS-DR8 data (Aihara et al. 2011) with galaxies in the redshift bin $0.0 < z < 0.1$ (light grey contours). We mark separately the distribution of those galaxies that satisfy the criterion $\text{EW}(H\alpha + [\text{N II}]) > 10 \text{ \AA}$ (dark grey contours) to guarantee star-forming objects similar to our sample. As the SDSS sample does not include B -band absolute magnitudes, we obtain them from $g' - B$ colours in Fukugita et al. (1995). The uncertainties that we considered were a 25% in the $[\text{O III}]/\text{H}\beta$ ratio (Guzmán et al. 1997) and 0.2 mag in the B -band absolute magnitude as in previous sections.

We show the rest-frame $\text{EW}([\text{O III}]\lambda 3727)$ versus luminosity diagram in Fig. 8. In this case, we employ the same mass bins

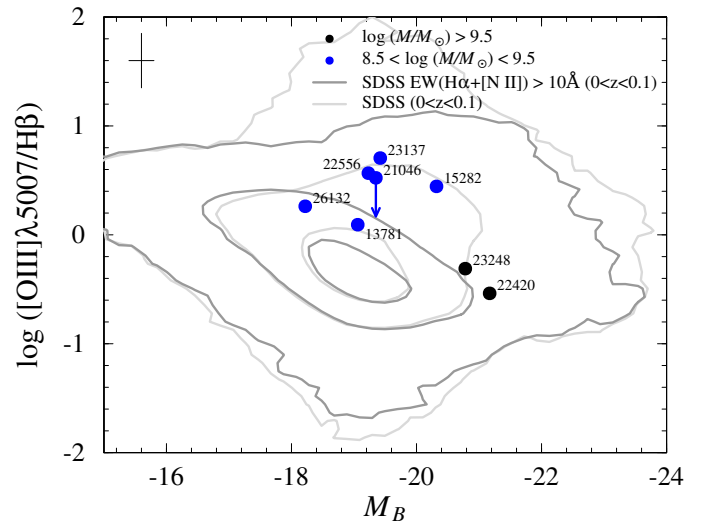


Fig. 7. Excitation vs. rest-frame B -band absolute magnitude. The sample is represented as filled circles with the mass differentiation in different colours as indicated in the legend. The SDSS reference is shown as grey lines with the contours corresponding to 99%, 75%, and 25%. Average error bars are located in the upper left corner.

and SDSS references as in Fig. 7. We assumed a typical 15% uncertainty in $\text{EW}_{\text{rf}}([\text{O II}])$ (Guzmán et al. 1997). This diagram provides information about the star formation of the galaxies. The $\text{EW}([\text{O II}])$ is used to obtain the $[\text{O II}]$ luminosities (Guzmán et al. 1997), a good tracer of the SFR (Kennicutt 1998). In addition, the EW is directly related with the burst strength. The higher the $\text{EW}([\text{O II}])$, the higher the burst strength. We can see that the lowest mass system has one of the highest $\text{EW}([\text{O II}])$. Low-mass systems of this kind are candidates for being galaxies dominated by the starburst. Intermediate-mass galaxies have similar $\text{EW}([\text{O II}])$ to the low-mass galaxies, but they have great dispersion. These intermediate-mass objects receive an important contribution from the burst. The high-mass galaxies present lower $\text{EW}([\text{O II}])$, they have an important contribution from the continuum, and have lower burst strengths.

In terms of the mass distinction, we find only one galaxy with $\log(M/M_\odot) < 8.5$, namely CANDELS 24623. This object has a mass $\log(M/M_\odot) = 7.91 \pm 0.08$, which is one of the lowest values in our sample. It is a clear star-forming object with a very prominent $[\text{O III}]\lambda 3727$ line and a very flat continuum (see Fig. 1). Its Spheroid(Compact) morphology and its high $\text{EW}_{\text{rf}}([\text{O II}]) = 96.8 \text{ \AA}$ indicate that it could be completely dominated by the starburst. This low-mass, low-luminosity ($M_B = -16.98$) galaxy is our best low metallicity candidate. It is the only object in our spectroscopic sample with these characteristics and has rest-frame colours $U - V = 0.58$ and $V - J = 0.11$.

In the intermediate-mass interval $8.5 < \log(M/M_\odot) < 9.5$, we find seven galaxies. These objects all show spectroscopic features corresponding to an $H\text{II}$ -like class (Guzmán et al. 1997) (see Fig. 1). They have intense emission lines with a flat continuum. In these cases $[\text{O III}]\lambda 5007 > \text{H}\beta$. They show low to intermediate metallicities. The best example of this class is CANDELS 23137, with prominent emission lines and featureless continuum. Its excitation is high ($\log([\text{O III}]/\text{H}\beta) = 0.71$), as is the $\text{EW}_{\text{rf}}([\text{O II}]) = 205.3 \text{ \AA}$, which is above the value of the low-mass galaxy 24623. CANDELS 15282 is the most massive of the galaxies in this mass bin with $\log(M/M_\odot) = 9.23 \pm 0.05$. Its properties are closer to the high-mass galaxies. CANDELS

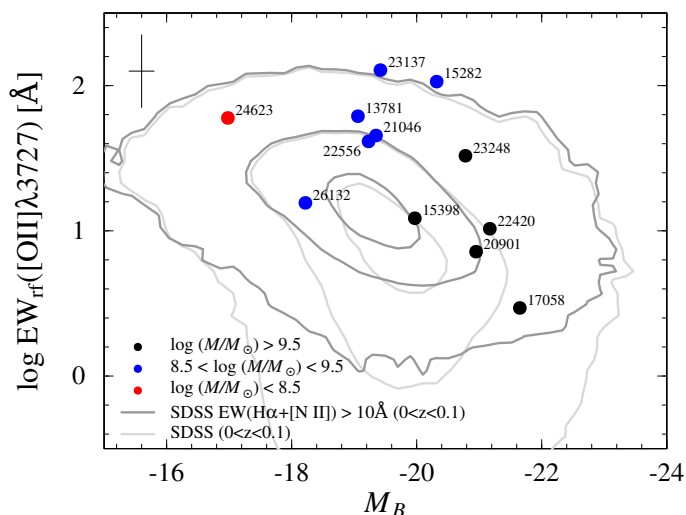


Fig. 8. Rest-frame [O III] EW vs. rest-frame B -band absolute magnitude. The sample is represented as filled circles. The mass bins are shown in different colours as indicated in the legend. The SDSS reference is shown as grey lines with contour levels 99%, 75%, and 25%. Average error bars are in the upper left corner.

21046 has an excitation value that does not correspond to its spectrum. The value that we get is higher than expected. With a detailed examination of its spectrum in Fig. 1 we discovered that a bad sky subtraction has eliminated a pixel in the $H\beta$ line. The $\text{FWHM}(H\beta) = 11.4 \text{ \AA}$ is below $\text{FWHM}([O III] \lambda 5007) = 28.3 \text{ \AA}$, which corresponds to the instrument profile width because the emission lines are not resolved. The estimated real value is indicated with an arrow in Fig. 7. CANDELS 21046 and 13781 have the lowest excitation in this category, a signature of an older burst in star formation. The two remaining objects CANDELS 22556 and 26132 have a very noisy spectra and we cannot give further information. $H\text{II}$ -like galaxies show average rest-frame colours $U - V = 0.83 \pm 0.29$ and $V - J = 0.44 \pm 0.30$.

The rest of the galaxies in the spectroscopic sample are in the high-mass bin $\log(M/M_\odot) > 9.5$. These five objects share characteristics related with a Disk-like class (Guzmán et al. 1997) as we can see in the Fig. 1 spectra. They have stronger $H\beta$ than [O III] and some absorption lines. These galaxies have higher metallicities than those in the previous categories. CANDELS 22420 and 23248 are the best cases in this Disk-like category. Their spectra show lower excitation with $H\beta > [O III]$. In addition, a clear Balmer break appears with absorption lines, indicative of an older stellar population. All of these features are well connected with Disk morphologies and redder postage stamps. The rest of the spectra in this class are very noisy and we had found it very difficult to perform a proper measurement of the lines. These galaxies are the most luminous ones with luminosities $M_B = [-19.97, -21.65]$ and masses ranging $\log(M/M_\odot) = [9.8, 10.4]$. Disk-like galaxies have average rest-frame colours $U - V = 1.13 \pm 0.18$ and $V - J = 1.00 \pm 0.18$.

4. $H\alpha$ luminosity function at $z \sim 0.62$

In this section we show our calculation of the $H\alpha$ -based LF at $z \sim 0.62$. This is a very important redshift in $H\alpha$ -based studies because no surveys cover the gap $0.5 < z < 0.8$. The LF determines how the SFR is distributed among the galaxy sample. First, we determined the observed LF. After that, we presented

the extinction-corrected LF. We corrected both of them for incompleteness. The objects employed for this purpose are those classified as $H\alpha$ emitters by their spec- z or photo- z at $z \sim 0.62$ as we indicated in Sect. 2.7. We have a $H\alpha$ SFGs sample of 28 objects.

To build our $H\alpha$ LF we employed the V/V_{max} method (Schmidt 1968). The number of galaxies per unit volume and interval $\Delta \log L$ is

$$\phi(\log L_i) = \frac{1}{\Delta \log L \cdot \Omega} \sum_j \frac{1}{V_j^{\text{max}}(z)}, \quad (9)$$

where L_i is the central luminosity in bin i of interval $\Delta \log L$, Ω is the solid angle of the survey, and $V_j^{\text{max}}(z)$ is the maximum volume in which we can detect the j object per unit solid angle.

We needed to obtain $V_j^{\text{max}}(z)$. The galaxies can be detected in the redshift interval of the NB filter effective width. This interval is $0.6098 < z < 0.6263$. The maximum volume of detection is the difference between the comoving volume at these redshifts. To calculate the comoving volume we used the *Milia* library again, which provided us this value per solid angle. As the survey field is $7.5' \times 7.5'$, the solid angle is $\Omega = 4.76 \times 10^{-6}$ sr. The maximum volume of detection for each galaxy is then $V_j^{\text{max}} = 2.57 \times 10^8 \text{ Mpc}^3 \text{ sr}^{-1}$. Hence, the volume covered by this survey is 1222 Mpc^3 . It is a smaller value than those used in other similar studies; for example Villar et al. (2008) at $z \sim 0.84$ has a $15.4' \times 15.4'$ field.

We used these values to build the LF. For the observed LF we chose a luminosity bin $\Delta \log L = 0.4 \text{ erg s}^{-1}$ and a first limit $\log L = 39.6 \text{ erg s}^{-1}$. These two values provide an optimal agreement between LF resolution and reliable statistics in the number of objects per bin. To determine the uncertainties in each bin we consider the process as Poissonian, so if the number of objects is N , the uncertainty is \sqrt{N} .

Next, we performed an extinction correction of the LF. A canonical extinction $A(H\alpha) = 1 \text{ mag}$ (Kennicutt 1992, 1998) is often applied in similar studies (e.g., Geach et al. 2008; Hayes et al. 2010; Sobral et al. 2012, 2013; Drake et al. 2013). Other authors argue that an extinction correction done individually for each object is a better approach (e.g., Ly et al. 2007; Westra & Jones 2008; Villar et al. 2008; Westra et al. 2010; Ly et al. 2011; Gunawardhana et al. 2013; An et al. 2014) as the extinction depends on redshift and on the luminosity of the galaxy, and affects the overall shape of the LF. Most luminous galaxies suffer higher extinctions flattening the shape of the faint end of the extinction-corrected LF (An et al. 2014). We decided to apply the most precise approach with the calculation of the extinction for each object individually as explained in Sect. 3.4. In this case, we operated with a bin $\Delta \log L = 0.4 \text{ erg s}^{-1}$ and a first limit $\log L = 40.0 \text{ erg s}^{-1}$.

For both observed and extinction-corrected LF we performed a correction for incompleteness. We followed the results obtained by our group in Villar et al. (2008), as indicated in Sect. 2.3. To take this effect into account, the fraction of simulated galaxies that meet our selection criteria is calculated. This is the so-called completeness fraction. The correction is based on assuming that this fraction is the probability that a galaxy will be detected and selected by our method. For each galaxy, we expect that the inverse of this fraction is the real number of galaxies. This is equivalent to multiplying the detection volume of each object by its completeness fraction. The factor is greater for the fainter sources.

In Figs. 9 and 10 we show both observed and extinction-corrected LFs along with the result once the incompleteness cor-

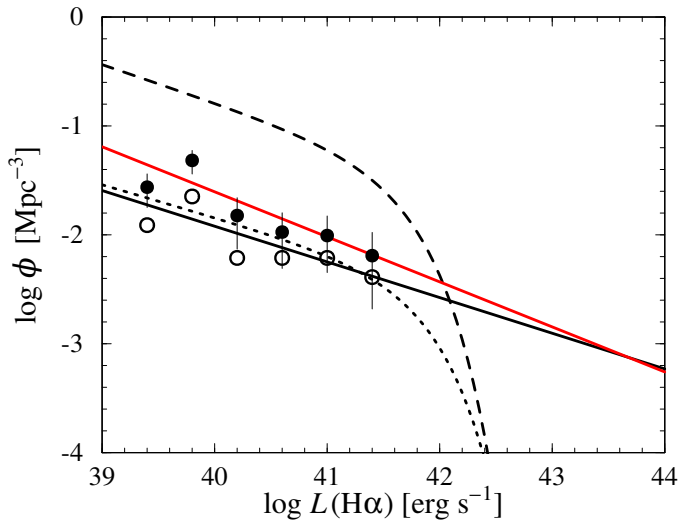


Fig. 9. Observed H α luminosity function at $z \sim 0.62$. We represent the LF corrected for incompleteness in black filled circles with the best linear fit as a red solid line. The open symbols indicate the LF values before applying this correction with the best linear fit as a black solid line. We also include as a reference the LF at $z \sim 0$ from Gallego et al. (1995) (black dotted line) and the observed LF at $z \sim 0.84$ from Villar et al. (2008) (black dashed line).

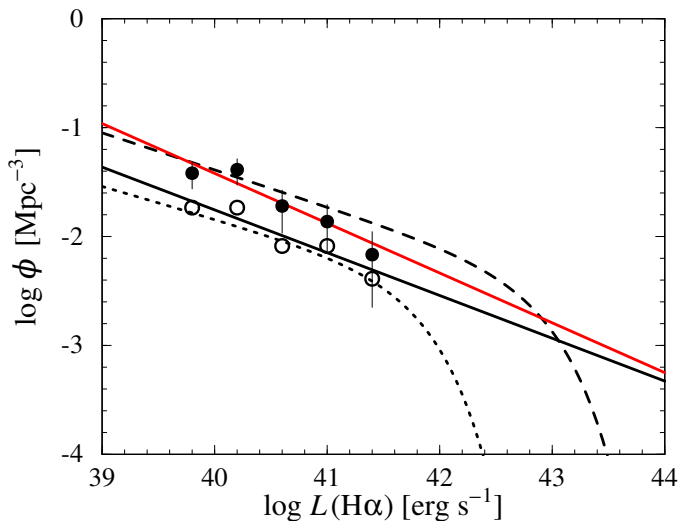


Fig. 10. Extinction-corrected H α luminosity function at $z \sim 0.62$. The LF corrected for incompleteness is shown as black filled circles along with the best linear fit as a red solid line. The LF values before applying the incompleteness correction are included as open symbols with the best linear fit as a black solid line. For comparison the LF at $z \sim 0$ from Gallego et al. (1995) (black dotted line) and the extinction-corrected LF at $z \sim 0.84$ from Villar et al. (2008) (black dashed line) are also shown.

rection is applied. In Table 4 we gather the number densities of the emitters for each luminosity bin. We see that the reddening correction moves the LF towards brighter values. Moreover, an individual treatment for each galaxy causes a redistribution of the objects in the luminosity bins. Because of this, we have a five-point LF in the corrected case instead of the six-point LF for the observed one. The incompleteness correction makes the LF move up, because it is more important for the faintest bins, and makes the LF steeper.

Table 4. Number densities of H α emitters for each luminosity bin.

log $L(\text{H}\alpha)$ (erg s $^{-1}$)	Extinction-corrected	Observed
	log ϕ (Mpc $^{-3}$)	log ϕ (Mpc $^{-3}$)
39.4	(...)	-1.56(-1.91) $^{+0.15}_{-0.23}$
39.8	-1.42(-1.74) $^{+0.12}_{-0.18}$	-1.32(-1.65) $^{+0.11}_{-0.16}$
40.2	-1.39(-1.74) $^{+0.12}_{-0.18}$	-1.82(-2.21) $^{+0.37}_{-0.30}$
40.6	-1.72(-2.09) $^{+0.18}_{-0.30}$	-1.97(-2.21) $^{+0.20}_{-0.37}$
41.0	-1.86(-2.09) $^{+0.18}_{-0.30}$	-2.01(-2.21) $^{+0.20}_{-0.37}$
41.4	-2.17(-2.39) $^{+0.23}_{-0.53}$	-2.19(-2.39) $^{+0.23}_{-0.53}$

Notes. We show both extinction-corrected and observed values after applying the incompleteness correction. In parentheses we also include the values before applying the incompleteness correction.

We were able to model the LF to a typical Schechter function (Schechter 1976; Gallego et al. 1995)

$$\phi(L)dL = \phi^* \left(\frac{L}{L^*}\right)^\alpha \exp\left(-\frac{L}{L^*}\right) \frac{dL}{L^*}, \quad (10)$$

where L^* is the characteristic galaxy luminosity where the power law form of the function cuts off. The parameter ϕ^* , in units of number density, provides the normalisation, and α is the faint-end slope of the LF. However, we note that there are no objects in the most luminous bins, the bright-end. We cannot trace the whole shape of the LF including the knee and the bright-end. We are limited to the faint end, nicely described by a power law. This issue is also present in other studies (Morioka et al. 2008; Hayes et al. 2010; An et al. 2014). The brighter the galaxy, the fewer there are. As a result, a higher number of brighter galaxies are gathered when covering larger areas. Our field is smaller than the fields used in similar studies. For instance, Villar et al. (2008) have a field approximately four times larger and they find around four times more objects. Consequently, they reach an extinction-corrected maximum luminosity bin of $\log L = 43.65$ erg s $^{-1}$ and trace the LF knee properly. This gain of two orders of magnitude is due to the larger volume that has been sampled and also because larger extinctions corrections for their brightest galaxies have been applied.

4.1. Faint end of the luminosity function

Our survey is extremely deep. A total integration time in the NB of 31.9 h led us to detect objects with fluxes $> 1.7 \times 10^{-18}$ erg s $^{-1}$ cm $^{-2}$. Considering only those objects classified as H α emitters at $z \sim 0.62$, the intrinsic H α luminosity reached is $> 2.9 \times 10^{39}$ erg s $^{-1}$. We were able to reach a very faint population of galaxies. Consequently, we measured extremely deep luminosity bins in the LF faint end. This part of the LF is a power law whose slope is directly $1 + \alpha$. We were able to measure a robust value of α with a simple linear fit. Robust values of α are only achievable through extremely deep surveys, like the one we conducted. In Figs. 9 and 10 we show a wide coverage of the LF faint end with six points in the observed case and five points in the extinction-corrected case.

We obtained four measurements of the α parameter. The values are listed in Table 5. First, we obtained the observed and extinction-corrected values as the result of a weighted linear fit. The α reddening-corrected value is larger than the observed one. Following an individual extinction correction for each galaxy, other studies suggest the opposite (Villar et al. 2008; An et al. 2014). The highest attenuated sources move to their actual high

Table 5. α values from LF faint-end linear fit.

	α
Extinction-corrected + incompleteness	$-1.46^{+0.16}_{-0.08}$
Extinction-corrected	$-1.39^{+0.18}_{-0.12}$
Observed + incompleteness	$-1.41^{+0.08}_{-0.15}$
Observed	$-1.33^{+0.15}_{-0.10}$

Notes. We collect the values of both the extinction-corrected and observed LFs, after and before applying the incompleteness correction.

luminosities flattening the LF and leading to a smaller α value. The reason for this discrepancy could depend on a different trend in terms of attenuation at the low luminosities that we trace in our work, that cover different ranges to those traced in the other studies (see Fig. 13). Another reason could be the use of LFs divided into luminosity bins. The objects move to higher luminosities when the extinction correction is applied, but not enough to populate a new and more luminous bin and thus to lead to a shallower result. Second, we obtained the α values corrected for incompleteness. The results are steeper owing to the nature of this correction as the faintest bins are more affected. In all cases, considering the uncertainties we measure, all the different values obtained here would be indistinguishable. We discuss these matters further in Sect. 5.

We calculated the uncertainties of the α parameters from Monte Carlo simulations. We computed ~ 10000 values. We varied each point of the LF with a Poisson probability distribution characterised by the λ parameter as the object detection follows a Poissonian process. The value of λ for each case was the number of objects in each bin. We performed a linear fit for every case and obtained the probability distribution of the parameter. The final uncertainties in the α parameters are the percentiles in the distributions within 68%, 1σ confidence level. This process should account for the binning effect on the α measurement.

5. Discussion

We discuss several considerations of our results in relation with similar studies. First of all, we want to treat the characterisation of the sample. Our ultra-deep observations led us to detect a wide variety of objects as we show through our morphological classification. These different categories of galaxies have different properties. In Table 6 we include the average values and deviations for several properties within the morphological categories. In this case, we only use the $H\alpha$ sample and the simplest version of the classification as we indicated in Sect. 3.1. We include Spheroidal galaxies and the Irregular CANDELS 15784 and 26460 in the Compact category. We combine the Spiral and Disk classes along with CANDELS 23137 into the same Disk. With this reduced classification 72% are Disk, 21% are Compact, 7% are Unclassifiable.

In terms of mass and size the Disk class shows the highest values with large deviations because this category includes a wide variety of disks. Disk is also the category with the highest luminosity and SFR. Thus, these galaxies dominate the brighter part of our LF. In contrast, Compact galaxies have very low masses and sizes, with low luminosities and SFRs. However, the higher $EW(H\alpha)$ and extinction that they present compared to the Disk galaxies is indicative and shows a more important contribution of the burst and higher dust content. In addition, as we noted in Sect. 3.1, the Sérsic index $n \sim 2$ is very distinctive of this Compact category. In addition to the two main

classes, we find two galaxies marked as Unclassifiable (CANDELS 17503 and 31370). These are very interesting objects as they show the lowest masses, luminosities, and SFRs with the highest extinctions. In terms of specific star formation rate (sSFR), the galaxies with the highest values are Compact galaxies with $sSFR(\text{Compact}) = 2.8 \pm 1.9 \text{ Gyr}^{-1}$, a much higher value than $sSFR(\text{Disk}) = 0.7 \pm 1.1 \text{ Gyr}^{-1}$ ($sSFR(\text{Unclassifiable}) = 2.3 \pm 0.7 \text{ Gyr}^{-1}$). The contribution of star formation in Compact galaxies relative to their mass is much more important than in the case of Disk galaxies. They are low-mass, compact, starburst-dominated systems. The epoch when low-mass SFGs form the bulk of their stellar mass is controversial. Rodríguez-Muñoz et al. (2015) find results that suggest a recent stellar mass assembly in agreement with cosmological downsizing (Cowie et al. 1996) from a sample of 31 spectroscopically confirmed galaxies at $0.3 < z < 0.9$ with masses $7.3 \leq \log(M/M_{\odot}) \leq 8.0$.

We can compare our sample with other works at different redshifts. Locally, Vitores et al. (1996) morphologically classified the UCM Survey sample. The results were 10% early types, 83% disks, 5% compacts, and 3% irregulars. These percentages are roughly similar to our results at $z \sim 0.62$. The population of SFGs in the universe at $z \sim 0.62$ is similar to local galaxies, morphologically speaking. The bulk of star formation appears to be contained within disks at these redshifts $0 < z < 0.62$. Previous studies have already shown that SFGs were dominated by disks at $z \sim 0.84$ (Villar et al. 2008; Sobral et al. 2009). For instance, the sample of SFGs from Sobral et al. (2009) is composed of 80% of disks. At $z \sim 1$ Konishi et al. (2011) found that star formation is mainly located on massive disk galaxies that are not triggered by early-phase galaxy-galaxy interactions disturbing the morphology in the NIR. The change from the locally similar scenario is found in studies at $z > 1$. Law et al. (2012) suggested that the picture of SFGs at $z \sim 2$ is consistent with gas-rich, compact, and triaxial systems dominated by velocity dispersion, rather than an axisymmetric disk view. The sample of ELGs at $z \sim 2.24$ from An et al. (2014) have a distribution of 45% that show signs of merger/interaction and just 23% of disks. This survey also has 18% of compact systems similar to ours, indicating that morphologies of this kind are present in a long stage of the cosmic history, with number percentages showing slight changes. Our ultra-deep survey allows us to detect very faint star formation regimes (i.e., $SFR < 0.1 M_{\odot} \text{ yr}^{-1}$) that are dominated by compact morphologies. Brough et al. (2011) studied a sample of faint $H\alpha$ emitters at $0.002 < z < 0.13$ with similar low stellar masses obtaining similar SFR and compact radii to ours. The difference in the percentages in the morphologies of these galaxies in other surveys is probably due to the depth of the study, but in general, the morphologies are similar in studies at $z < 1$. This is also an argument in favour of narrow-band surveys like ours. Covering smaller volumes and detecting a smaller number of galaxies, it detects a representative sample of the morphologies in the universe at the studied redshift.

In Sect. 4.1 we calculated the LF faint-end slope by performing a linear fit. This is done under the assumption that none of the LF points are tracing the LF knee or the bright-end. They all lie in the LF regime that is accurately described by a power law. According to the results from Gallego et al. (1995) and Villar et al. (2008) this is a safe assumption (see Figs. 9 and 10). However, it is worth discussing what the result would be if we did not make this previous supposition and if we fit a typical Schechter function (Schechter 1976). A simple way to do this with our data is by fixing the characteristic luminosity L^* and by fitting ϕ^* and α . Sobral et al. (2013) propose $\log L^*(H\alpha)(z) = 0.45z + 41.87$ as an evolution law for $L^*(H\alpha)$ with redshift. At $z \sim 0.62$,

Table 6. Average values and deviations of several physical properties for the ‘ $H\alpha$ ’ sample.

Category	$\log(M/M_\odot)$	$\log r_e$ (kpc)	n^a	M_B	$EW_{\text{rf}}(H\alpha)$ (Å)	$A(H\alpha)$ (mag)	SFR_{cor} ($M_\odot \text{ yr}^{-1}$)
Disk (72%)	8.94 ± 0.85	-0.40 ± 0.20	0.92 ± 0.31	-18.88 ± 1.69	61 ± 140	0.40 ± 0.34	0.52 ± 0.81
Compact (21%)	7.71 ± 0.22	-0.70 ± 0.10	1.87 ± 0.87	-16.24 ± 0.65	141 ± 250	0.97 ± 0.65	0.13 ± 0.07
Unclassifiable (7%)	7.54 ± 0.06	-0.49 ± 0.14	(...)	-15.16 ± 0.07	91 ± 40	1.24 ± 0.27	0.08 ± 0.01

Notes. ^(a) The Sérsic index values only consider the objects with structural parameters available in van der Wel et al. (2012).

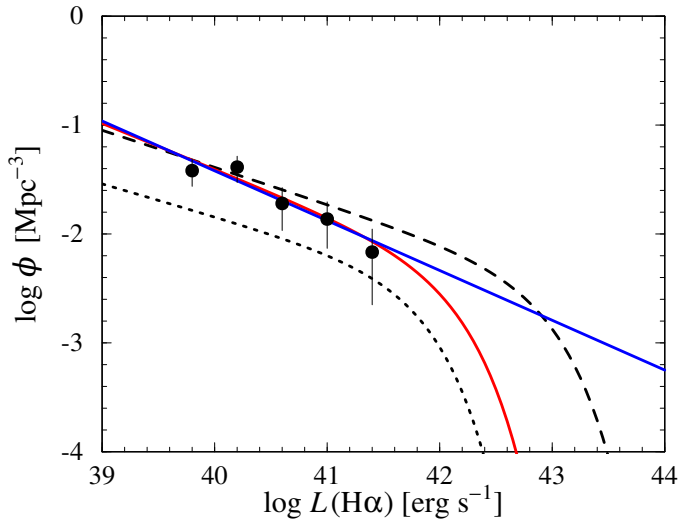


Fig. 11. Extinction and incompleteness corrected $H\alpha$ luminosity function at $z \sim 0.62$. The best Schechter function fit is shown as a red solid line and the best linear fit as a blue solid line. LF at $z \sim 0$ from Gallego et al. (1995) (black dotted line) and the extinction-corrected LF at $z \sim 0.84$ from Villar et al. (2008) (black dashed line) are also included.

$\log L^*(H\alpha) = 42.15 \text{ erg s}^{-1}$. A Schechter fit leads us to the following parameters where the uncertainties come from Monte Carlo realisations, as in the α linear fit: $\phi^* = 10^{-2.67^{+0.29}_{-0.18}} \text{ Mpc}^{-3}$ and $\alpha = -1.42^{+0.15}_{-0.09}$. The α value obtained in this way is similar to those presented in Table 5 calculated with a linear fit. This confirms that the assumption made in Sect. 4.1 is correct. In Fig. 11 we show the output of this approach.

We can compare the α values we calculate in this work with the values in the literature. We detect objects with fluxes $> 1.7 \times 10^{-18} \text{ erg s}^{-1} \text{ cm}^{-2}$, thus reaching luminosity bins $> \log L = 39.4 \text{ erg s}^{-1}$ ($> \log L = 39.8 \text{ erg s}^{-1}$ extinction-corrected). We can robustly obtain a value of the α parameter. In Fig. 12 we plot the evolution of α with redshift from several literature studies along with our result from a linear fit and corrected for extinction and incompleteness. We clearly see two trends: a non-evolving $\alpha = -1.3$ (Gallego et al. 1995; Pérez-González et al. 2003; Westra & Jones 2008; Villar et al. 2008; An et al. 2014) and a non-evolving $\alpha = -1.6$ (Ly et al. 2007, 2011; Sobral et al. 2012) with redshift. An et al. (2014) suggest that this difference is mostly explained as the result of applying an individual extinction correction for each galaxy ($\alpha = -1.3$) or using a canonical value $A(H\alpha) = 1 \text{ mag}$ ($\alpha = -1.6$). These authors argue that an individual extinction correction is vital in the shape of the $H\alpha$ LF, as a constant value tends to overestimate the effect in the faint end of the LF and to underestimate it in the bright end, which causes a steeper α .

Our results suggest that correcting for extinction for each object individually goes in the opposite direction and produces a

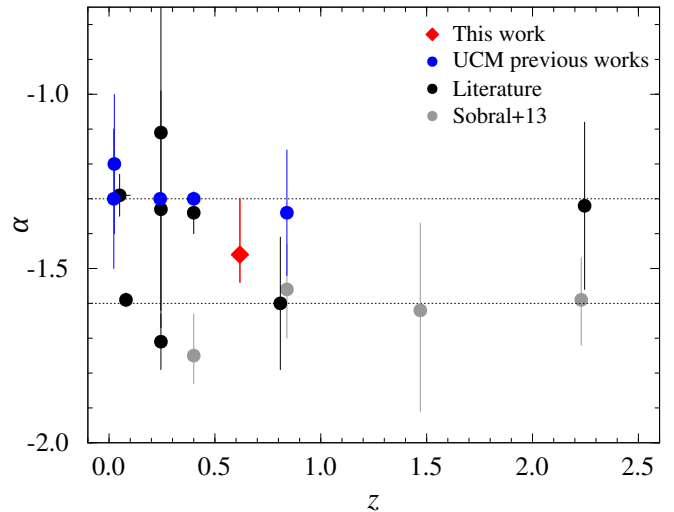


Fig. 12. Evolution of the α parameter as calculated by several studies in the literature along with our result. This work is shown as red filled diamonds. We present the extinction + incompleteness corrected value obtained through a linear fit. We emphasise previous UCM works as blue filled circles. (Pascual et al. (2001); Pascual (2005) fix the $\alpha = -1.3$ value). The black circles designate several studies from the literature: at $z < 0.1$ Gunawardhana et al. (2015); at $z \sim 0.24$ Westra & Jones (2008), Ly et al. (2007) $z < 0.4$, and Ly et al. (2011) $z \sim 0.8$; and at $z \sim 2.24$ An et al. (2014). The evolution from Sobral et al. (2013) at $z \sim 0.4, 0.84, 1.47, 2.23$ is shown as grey filled circles.

steeper α (see Table 5). The reason for this discrepancy could be a real physical difference in the galaxy population in terms of attenuation at the lowest luminosities. Nevertheless, we have to take into account the resolution in our LF that is due to the choice of the luminosity bins. The objects move to higher luminosities when the extinction correction is applied, but not enough to populate a new and more luminous bin leading to a steeper result. By performing Monte Carlo realisations to get the uncertainties we are accounting for this effect. It is important to note that the α results presented in Table 5 and the values given by An et al. (2014) ($\alpha = -1.32 \pm 0.24$) are indistinguishable within the uncertainties. If there is a physical origin in the discrepancy, in order to explain the steeper α after applying an individual extinction correction the galaxies with lower luminosities would be the ones with higher extinctions (see Table 6). The objects with lower luminosities as shown by M_B are the ones with higher extinctions. In Fig. 13 we explore this further by plotting the extinction as a function of the $H\alpha$ luminosity. Covering different luminosity ranges to those used in our work, we do not see the same trend in the sample from Villar et al. (2008) and Fig. 10 in An et al. (2014). In these works the higher the luminosity, the higher the extinction. However, in our work we see that the galaxies with the highest luminosities do not present the highest extinctions.

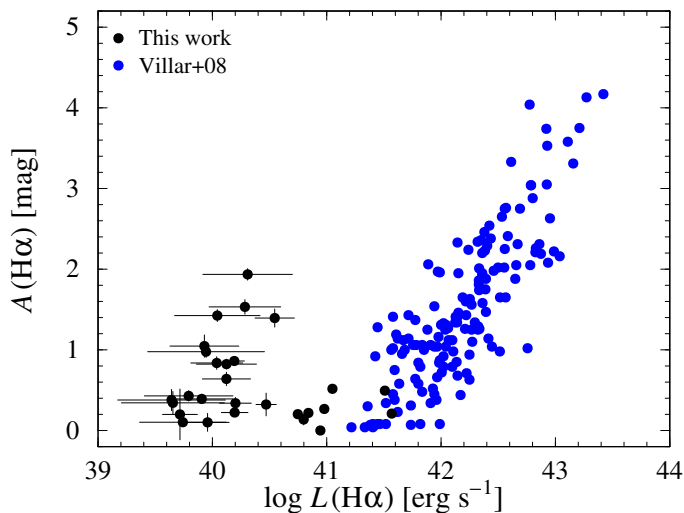


Fig. 13. $H\alpha$ extinction vs. $H\alpha$ luminosity. The objects in our sample are shown as black filled circles and the ones from Villar et al. (2008) at $z \sim 0.84$ as blue filled circles.

In fact, the objects with the highest extinctions have much lower luminosities. This could explain why we obtain a steeper value in the LF faint-end slope. As a sanity check we verify that we get the same behaviour for our objects when comparing the $H\alpha$ extinction with M_B because the M_B values are independent from our measurements.

Additionally, we can calculate the $H\alpha$ luminosity density,

$$\rho_L(H\alpha) = \phi^* L^* \Gamma(2 + \alpha), \quad (11)$$

from the Schechter parameters previously obtained. This result can be converted to SFRD through the Kennicutt (1998) calibration. We get a value of $\rho_{\text{SFR}} = 0.036^{+0.012}_{-0.008} M_{\odot} \text{ yr}^{-1} \text{ Mpc}^{-3}$. We put our result in the context of the SFRD evolution in Fig. 14. The result follows the trend established by previous works in the literature. We include the $H\alpha$ -based SFRD compilation in Table B1 of Gunawardhana et al. (2013), as well as the values calculated by these authors in the redshift range $z < 0.35$ (Gunawardhana et al. 2013, 2015). We substitute the values from GAMA data at $z > 0.1$ for the newly calculated values in Gunawardhana et al. (2015). In addition, we add the most recent works not included in the mentioned compilation (Sobral et al. 2012, 2013; Drake et al. 2013; Sobral et al. 2015; Stroe & Sobral 2015). All studies here are compared assuming a common concordance cosmology, Salpeter IMF, and applying an extinction correction (Gunawardhana et al. 2013). Our work is the first conducted in $H\alpha$ at $z \sim 0.6$, connecting and filling the gap between $0.5 < z < 0.8$ studies.

6. Summary

In this project we selected a sample of 28 star-forming galaxies at $z \sim 0.62$ from their $H\alpha$ emission. We employed narrow-band ultra-deep VLT/HAWK-I observations, for a total of 31.9 h in this filter centred at $1.06 \mu\text{m}$. The main goal of this work is to study the properties of the resulting sample of faint $H\alpha$ emitters at $z \sim 0.62$. We mainly focus on their contribution to the faint end of the luminosity function and we derived the star formation rate density. We also characterised their morphologies and basic photometric and spectroscopic properties. In studies of this kind $z \sim 0.62$ is an important redshift region; there is a gap in $0.5 <$

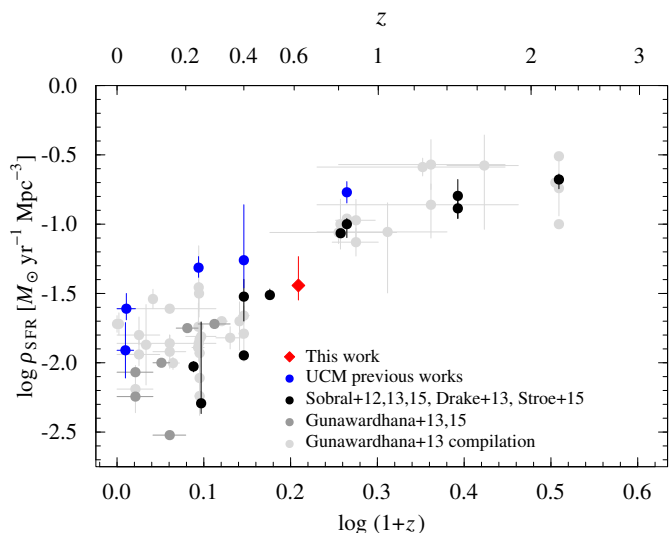


Fig. 14. Evolution of the SFRD with redshift from $H\alpha$ studies. This work is shown as red filled diamond. We indicate previous UCM works as blue filled circles. The black circles correspond to the studies of Sobral et al. (2012) at $z \sim 1.47$; Sobral et al. (2013) at $z \sim 0.4, 0.84, 1.47, 2.23$; Drake et al. (2013) at $z \sim 0.25, 0.4, 0.5$; Sobral et al. (2015) at $z \sim 0.8$; and Stroe & Sobral (2015) at $z \sim 0.2$. The compilation in Table B1 of Gunawardhana et al. (2013) is included as grey filled circles. The results in Table 2 of Gunawardhana et al. (2013) for the redshift bins $0.1 < z < 0.15$, $0.17 < z < 0.24$, and $0.24 < z < 0.35$.

$z < 0.8$ $H\alpha$ works due to the efficiency problems in the detector transition from optical to near-infrared.

- We characterised the sample. Morphologically, we collected a disk-dominated sample (79%) with an important contribution from compact galaxies (21%). This is consistent with a local scenario of disk systems dominating the bulk of star-forming galaxies at $0 < z < 1$.
- The star formation rate is higher in disks, but the specific star formation rate is greater in compact morphologies. These galaxies are low-mass, compact, starburst-dominated systems. The structural parameter analysis shows light profiles in an intermediate stage from early- to late-types because they have Sérsic indexes $n \sim 2$.
- We calculated a robust value for the faint-end slope of the luminosity function $\alpha = -1.46^{+0.16}_{-0.08}$, applying an individual extinction correction for each galaxy in the sample and taking into account the incompleteness factor.
- The extinction is lower in the emitters with the highest $H\alpha$ luminosity than in fainter sources within the sample. This could explain the steeper α value obtained after individually correcting each object for extinction.
- We obtained an extinction-corrected star formation rate density $\rho_{\text{SFR}} = 0.036^{+0.012}_{-0.008} M_{\odot} \text{ yr}^{-1} \text{ Mpc}^{-3}$ at $z \sim 0.62$. This result is consistent with the evolution of this parameter with cosmic history as shown in the literature.

Acknowledgements. We would like to thank the anonymous referee whose valuable comments have improved this work. We acknowledge support from the Spanish Programa Nacional de Astronomía y Astrofísica: projects AYA2013-46724-P, AYA2012-30717, and AYA2009-10368. This work has made use of the Rainbow Cosmological Surveys Database, which is operated by the Universidad Complutense de Madrid (UCM), partnered with the University of California Observatories at Santa Cruz (UCO/Lick,UCSC). We are very grateful to Pablo G.

Pérez-González for his technical advice on Rainbow usage and its data. We thank Guillermo Barro for helping with the stellar masses catalogue, discussions, and last details and Michael Cooper for kindly providing his available spectra for our sample. We thank Nicolás Cardiel, Omaira González-Martín, and Sune Toft for useful comments and advice. C.G.G acknowledges funding by the Spanish Beca de Colaboración 2013-2014 programme.

References

- Aihara, H., Allende Prieto, C., An, D., et al. 2011, *ApJS*, 193, 29
- An, F. X., Zheng, X. Z., Wang, W.-H., et al. 2014, *ApJ*, 784, 152
- Baldwin, J. A., Phillips, M. M., & Terlevich, R. 1981, *PASP*, 93, 5
- Balestra, I., Mainieri, V., Popesso, P., et al. 2010, *A&A*, 512, A12
- Barro, G., Pérez-González, P. G., Gallego, J., et al. 2011a, *ApJS*, 193, 13
- Barro, G., Pérez-González, P. G., Gallego, J., et al. 2011b, *ApJS*, 193, 30
- Beckwith, S. V. W. 2005, *VizieR Online Data Catalog*, 2258, 0
- Behroozi, P. S., Wechsler, R. H., & Conroy, C. 2013, *ApJ*, 770, 57
- Brinchmann, J., Charlot, S., White, S. D. M., et al. 2004, *MNRAS*, 351, 1151
- Brough, S., Hopkins, A. M., Sharp, R. G., et al. 2011, *MNRAS*, 413, 1236
- Buat, V., Iglesias-Páramo, J., Seibert, M., et al. 2005, *ApJ*, 619, L51
- Calzetti, D., Armus, L., Bohlin, R. C., et al. 2000, *ApJ*, 533, 682
- Casali, M., Pirard, J.-F., Kissler-Patig, M., et al. 2006, in *Society of Photo-Optical Instrumentation Engineers (SPIE) Conference Series*, Vol. 6269, Society of Photo-Optical Instrumentation Engineers (SPIE) Conference Series, 0
- Clément, B., Cuby, J.-G., Courbin, F., et al. 2012, *A&A*, 538, A66
- Cooper, M. C., Yan, R., Dickinson, M., et al. 2012, *MNRAS*, 425, 2116
- Cowie, L. L., Songaila, A., Hu, E. M., & Cohen, J. G. 1996, *AJ*, 112, 839
- Dahlen, T., Mobasher, B., Faber, S. M., et al. 2013, *ApJ*, 775, 93
- Dale, D. A., Barlow, R. J., Cohen, S. A., et al. 2010, *ApJ*, 712, L189
- Doherty, M., Bunker, A., Sharp, R., et al. 2006, *MNRAS*, 370, 331
- Dopita, M. A. & Evans, I. N. 1986, *ApJ*, 307, 431
- Drake, A. B., Simpson, C., Collins, C. A., et al. 2013, *MNRAS*, 433, 796
- Elbaz, D., Dickinson, M., Hwang, H. S., et al. 2011, *A&A*, 533, A119
- Fujita, S. S., Ajiki, M., Shioya, Y., et al. 2003, *ApJ*, 586, L115
- Fukugita, M., Shimasaku, K., & Ichikawa, T. 1995, *PASP*, 107, 945
- Gallego, J., Zamorano, J., Aragon-Salamanca, A., & Rego, M. 1995, *ApJ*, 455, L1
- Gallego, J., Zamorano, J., Rego, M., & Vitores, A. G. 1997, *ApJ*, 475, 502
- Geach, J. E., Smail, I., Best, P. N., et al. 2008, *MNRAS*, 388, 1473
- Glazebrook, K., Blake, C., Economou, F., Lilly, S., & Colless, M. 1999, *MNRAS*, 306, 843
- Glazebrook, K., Tober, J., Thomson, S., Bland-Hawthorn, J., & Abraham, R. 2004, *AJ*, 128, 2652
- Grogin, N. A., Kocevski, D. D., Faber, S. M., et al. 2011, *ApJS*, 197, 35
- Gunawardhana, M. L. P., Hopkins, A. M., Bland-Hawthorn, J., et al. 2013, *MNRAS*, 433, 2764
- Gunawardhana, M. L. P., Hopkins, A. M., Taylor, E. N., et al. 2015, *MNRAS*, 447, 875
- Guo, Y., Ferguson, H. C., Giavalisco, M., et al. 2013, *ApJS*, 207, 24
- Guzmán, R., Gallego, J., Koo, D. C., et al. 1997, *ApJ*, 489, 559
- Hanish, D. J., Meurer, G. R., Ferguson, H. C., et al. 2006, *ApJ*, 649, 150
- Hao, C.-N., Kennicutt, R. C., Johnson, B. D., et al. 2011, *ApJ*, 741, 124
- Hayes, M., Schaerer, D., & Östlin, G. 2010, *A&A*, 509, L5
- Hippelein, H., Maier, C., Meisenheimer, K., et al. 2003, *A&A*, 402, 65
- Hopkins, A. M. 2004, *ApJ*, 615, 209
- Hopkins, A. M. & Beacom, J. F. 2006, *ApJ*, 651, 142
- Hopkins, A. M., Connolly, A. J., & Szalay, A. S. 2000, *AJ*, 120, 2843
- James, P. A., Knapen, J. H., Shane, N. S., Baldry, I. K., & de Jong, R. S. 2008, *A&A*, 482, 507
- Karachentsev, I. D. & Kaisin, S. S. 2010, *AJ*, 140, 1241
- Kartaltepe, J. S., Mozena, M., Kocevski, D., et al. 2015, *ApJS*, 221, 11
- Kennicutt, R. C. & Evans, N. J. 2012, *ARA&A*, 50, 531
- Kennicutt, Jr., R. C. 1992, *ApJ*, 388, 310
- Kennicutt, Jr., R. C. 1998, *ARA&A*, 36, 189
- Kissler-Patig, M., Pirard, J.-F., Casali, M., et al. 2008, *A&A*, 491, 941
- Kochiashvili, I., Møller, P., Milvang-Jensen, B., et al. 2015, *A&A*, 580, A42
- Koekemoer, A. M., Faber, S. M., Ferguson, H. C., et al. 2011, *ApJS*, 197, 36
- Konishi, M., Akiyama, M., Kajisawa, M., et al. 2011, *PASJ*, 63, 363
- Law, D. R., Steidel, C. C., Shapley, A. E., et al. 2012, *ApJ*, 745, 85
- Le Fèvre, O., Vettolani, G., Paltani, S., et al. 2004, *A&A*, 428, 1043
- Lilly, S. J., Le Fèvre, O., Hammer, F., & Crampton, D. 1996, *ApJ*, 460, L1
- Ly, C., Lee, J. C., Dale, D. A., et al. 2011, *ApJ*, 726, 109
- Ly, C., Malkan, M. A., Kashikawa, N., et al. 2007, *ApJ*, 657, 738
- Madau, P. & Dickinson, M. 2014, *ARA&A*, 52, 415
- Madau, P., Ferguson, H. C., Dickinson, M. E., et al. 1996, *MNRAS*, 283, 1388
- Magnelli, B., Popesso, P., Berta, S., et al. 2013, *A&A*, 553, A132
- Marino, R. A., Rosaes-Ortega, F. F., Sánchez, S. F., et al. 2013, *A&A*, 559, A114
- Moorwood, A. F. M., van der Werf, P. P., Cuby, J. G., & Oliva, E. 2000, *A&A*, 362, 9
- Morioka, T., Nakajima, A., Taniguchi, Y., et al. 2008, *PASJ*, 60, 1219
- Muñoz-Mateos, J. C., Gil de Paz, A., Boissier, S., et al. 2009, *ApJ*, 701, 1965
- Nakamura, O., Fukugita, M., Brinkmann, J., & Schneider, D. P. 2004, *AJ*, 127, 2511
- Oke, J. B. 1974, *ApJS*, 27, 21
- Oteo, I., Sobral, D., Ivison, R. J., et al. 2015, *MNRAS*, 452, 2018
- Pascual, S. 2005, *PASP*, 117, 120
- Pascual, S. 2015, *milia: version 1.0.0*
- Pascual, S., Gallego, J., Aragon-Salamanca, A., & Zamorano, J. 2001, *A&A*, 379, 798
- Pascual, S., Gallego, J., & Zamorano, J. 2007, *PASP*, 119, 30
- Patel, S. G., Holden, B. P., Kelson, D. D., et al. 2012, *ApJ*, 748, L27
- Pérez-González, P. G., Egami, E., Rex, M., et al. 2010, *A&A*, 518, L15
- Pérez-González, P. G., Rieke, G. H., Egami, E., et al. 2005, *ApJ*, 630, 82
- Pérez-González, P. G., Rieke, G. H., Villar, V., et al. 2008a, *ApJ*, 675, 234
- Pérez-González, P. G., Trujillo, I., Barro, G., et al. 2008b, *ApJ*, 687, 50
- Pérez-González, P. G., Zamorano, J., Gallego, J., Aragon-Salamanca, A., & Gil de Paz, A. 2003, *ApJ*, 591, 827
- Pettini, M. & Pagel, B. E. J. 2004, *MNRAS*, 348, L59
- Phillips, A. C., Guzmán, R., Gallego, J., et al. 1997, *ApJ*, 489, 543
- Pirard, J.-F., Kissler-Patig, M., Moorwood, A., et al. 2004, in *Society of Photo-Optical Instrumentation Engineers (SPIE) Conference Series*, Vol. 5492, Ground-based Instrumentation for Astronomy, ed. A. F. M. Moorwood & M. Iye, 1763–1772
- Rodríguez-Muñoz, L., Gallego, J., Pacifici, C., et al. 2015, *ApJ*, 799, 36
- Santini, P., Ferguson, H. C., Fontana, A., et al. 2015, *ApJ*, 801, 97
- Schechter, P. 1976, *ApJ*, 203, 297
- Schlafly, E. F. & Finkbeiner, D. P. 2011, *ApJ*, 737, 103
- Schmidt, M. 1968, *ApJ*, 151, 393
- Shim, H., Colbert, J., Teplitz, H., et al. 2009, *ApJ*, 696, 785
- Shioya, Y., Taniguchi, Y., Sasaki, S. S., et al. 2008, *ApJS*, 175, 128
- Siebenmorgen, R., Carraro, G., Valenti, E., et al. 2011, *The Messenger*, 144, 9
- Skelton, R. E., Whitaker, K. E., Momcheva, I. G., et al. 2014, *ApJS*, 214, 24
- Sobral, D., Best, P. N., Geach, J. E., et al. 2009, *MNRAS*, 398, 75
- Sobral, D., Best, P. N., Matsuda, Y., et al. 2012, *MNRAS*, 420, 1926
- Sobral, D., Matthee, J., Best, P. N., et al. 2015, *MNRAS*, 451, 2303
- Sobral, D., Smail, I., Best, P. N., et al. 2013, *MNRAS*, 428, 1128
- Stroe, A. & Sobral, D. 2015, *MNRAS*, 453, 242
- Sullivan, M., Treyer, M. A., Ellis, R. S., et al. 2000, *MNRAS*, 312, 442
- Tadaki, K.-I., Kodama, T., Koyama, Y., et al. 2011, *PASJ*, 63, 437
- Tresse, L. & Maddox, S. J. 1998, *ApJ*, 495, 691
- Tresse, L., Maddox, S. J., Le Fèvre, O., & Cuby, J.-G. 2002, *MNRAS*, 337, 369
- van der Wel, A., Bell, E. F., Häussler, B., et al. 2012, *ApJS*, 203, 24
- Vanzella, E., Cristiani, S., Dickinson, M., et al. 2008, *A&A*, 478, 83
- Veilleux, S. & Osterbrock, D. E. 1987, *ApJS*, 63, 295
- Vilella-Rojo, G., Viironen, K., López-Sanjuan, C., et al. 2015, *A&A*, 580, A47
- Villar, V., Gallego, J., Pérez-González, P. G., et al. 2008, *ApJ*, 677, 169
- Vitores, A. G., Zamorano, J., Rego, M., Gallego, J., & Alonso, O. 1996, *A&AS*, 120, 385
- Westra, E., Geller, M. J., Kurtz, M. J., Fabricant, D. G., & Dell’Antonio, I. 2010, *ApJ*, 708, 534
- Westra, E. & Jones, D. H. 2008, *MNRAS*, 383, 339
- Williams, R. J., Quadri, R. F., Franx, M., van Dokkum, P., & Labbé, I. 2009, *ApJ*, 691, 1879
- Xue, Y. Q., Luo, B., Brandt, W. N., et al. 2011, *ApJS*, 195, 10
- Yan, L., McCarthy, P. J., Freudling, W., et al. 1999, *ApJ*, 519, L47
- Zamorano, J., Gallego, J., Rego, M., Vitores, A. G., & Alonso, O. 1996, *ApJS*, 105, 343
- Zamorano, J., Rego, M., Gallego, J. G., et al. 1994, *ApJS*, 95, 387

Table 3. Sample data.

ID	$\alpha(J2000)$ (deg)	$\delta(J2000)$ (deg)	z_{phot}	z_{spec}	Line ^d	$\log(M/M_{\odot})$	f_i (10^{-18} erg s ⁻¹ cm ⁻²)	EW(H α) (Å)	A(H α) (mag)	SFR _{cor} (M_{\odot} yr ⁻¹)	Morphology
12039	53.097336	-27.800426	0.42 ± 0.15	(...)	H α	7.59 ± 0.09	2.7 ± 0.5	1038.9 ± 290.6	0.20 ± 0.31	0.04 ± 0.01	Disk
13781	53.168017	-27.789670	0.59 ± 0.30	0.619	H α	8.98 ± 0.04	34.5 ± 2.0	63.7 ± 4.6	0.14 ± 0.07	0.50 ± 0.04	Spiral
15282	53.158169	-27.781095	0.59 ± 0.30	0.620	H α	9.23 ± 0.05	54.5 ± 2.2	76.2 ± 4.1	0	0.70 ± 0.03	Spiral
15286	53.172260	-27.779516	0.65 ± 0.33	(...)	H α	8.19 ± 0.07	3.5 ± 2.2	38.5 ± 26.3	0.40 ± 0.06	0.06 ± 0.04	Disk
15398	53.172609	-27.780967	0.57 ± 0.29	0.619	H α	9.90 ± 0.08	43.3 ± 2.4	36.2 ± 2.2	0.52 ± 0.06	0.89 ± 0.07	Spiral
15784	53.178185	-27.775894	0.60 ± 0.31	(...)	H α	7.82 ± 0.06	2.9 ± 2.1	33.1 ± 25.3	1.53 ± 0.09	0.15 ± 0.11	Irregular
16155	53.168582	-27.772930	0.56 ± 0.29	(...)	H α	7.79 ± 0.08	2.1 ± 1.9	65.4 ± 73.2	1.94 ± 0.07	0.16 ± 0.14	Spheroidal
16644	53.172101	-27.770380	0.54 ± 0.28	(...)	H α	9.01 ± 0.06	2.2 ± 2.6	8.4 ± 10.0	0.98 ± 0.07	0.07 ± 0.08	Disk
16839	53.153536	-27.769445	0.51 ± 0.26	(...)	H α	8.96 ± 0.12	1.9 ± 2.1	14.3 ± 15.6	0.38 ± 0.13	0.03 ± 0.04	Disk
16845	53.064759	-27.767741	0.66 ± 0.34	(...)	H α	7.97 ± 0.05	4.6 ± 2.2	66.5 ± 40.7	0.64 ± 0.08	0.10 ± 0.05	Disk
17058	53.169925	-27.771024	0.61 ± 0.31	0.622	H α	10.39 ± 0.07	34.8 ± 2.6	18.6 ± 1.4	0.22 ± 0.03	0.55 ± 0.04	Spiral
17503	53.114224	-27.762464	0.62 ± 0.32	(...)	H α	7.58 ± 0.15	2.0 ± 1.4	195.1 ± 315.6	1.05 ± 0.14	0.07 ± 0.05	Unclassifiable
18482	53.139078	-27.753542	0.87 ± 0.44	(...)	H α	7.97 ± 0.07	3.1 ± 1.6	150.5 ± 155.6	0.84 ± 0.08	0.09 ± 0.04	Disk
19256	53.110459	-27.747339	0.38 ± 0.20	(...)	H α	7.77 ± 0.06	2.0 ± 2.1	40.9 ± 46.7	0.34 ± 0.14	0.04 ± 0.04	Spheroidal
20380	53.177126	-27.737653	0.70 ± 0.36	(...)	H α	8.54 ± 0.10	7.9 ± 2.1	44.9 ± 13.3	0.22 ± 0.05	0.12 ± 0.03	Disk
20901	53.190161	-27.734945	0.60 ± 0.31	0.619	H α	10.11 ± 0.07	46.3 ± 2.8	23.3 ± 1.5	0.27 ± 0.04	0.75 ± 0.05	Spiral
21046	53.116710	-27.732614	0.54 ± 0.28	0.621	H α	9.14 ± 0.08	28.6 ± 2.3	59.4 ± 5.8	0.20 ± 0.04	0.44 ± 0.04	Disk
21360	53.106294	-27.727954	0.63 ± 0.32	(...)	H α	8.12 ± 0.10	2.6 ± 2.3	27.1 ± 25.3	0.43 ± 0.07	0.05 ± 0.04	Disk
22420	53.097519	-27.721271	0.58 ± 0.30	0.615	H α	10.40 ± 0.09	129.2 ± 2.4	34.5 ± 0.7	0.49 ± 0.04	2.55 ± 0.11	Spiral
22556	53.063490	-27.720247	0.59 ± 0.30	0.609	H α	9.07 ± 0.06	5.3 ± 2.3	12.6 ± 5.4	0.10 ± 0.11	0.07 ± 0.03	Disk
22962	53.142643	-27.708699	0.55 ± 0.28	(...)	H α	7.90 ± 0.10	7.2 ± 2.3	144.3 ± 90.1	0.34 ± 0.06	0.13 ± 0.04	Disk
23065	53.152421	-27.706515	0.68 ± 0.35	(...)	H α	7.29 ± 0.09	4.4 ± 0.9	1038.9 ± 289.5	0.86 ± 0.05	0.12 ± 0.02	Compact
23137	53.077383	-27.708195	0.57 ± 0.29	0.605	H α	8.73 ± 0.05	3.3 ± 2.9	6.5 ± 5.7	0.10 ± 0.04	0.04 ± 0.04	Irregular
23248	53.141244	-27.710543	0.61 ± 0.31	0.619	H α	9.80 ± 0.03	189.8 ± 2.9	77.9 ± 1.6	0.21 ± 0.04	2.93 ± 0.13	Disk
24623	53.174256	-27.678432	0.60 ± 0.31	0.616	H α	7.91 ± 0.08	13.8 ± 2.2	104.8 ± 25.4	0.32 ± 0.14	0.23 ± 0.05	Spheroidal
26132	53.131199	-27.699450	0.60 ± 0.31	0.620	H α	8.76 ± 0.04	6.0 ± 2.3	22.0 ± 8.7	1.39 ± 0.11	0.28 ± 0.11	Disk
26460	53.144189	-27.703179	0.71 ± 0.36	(...)	H α	7.66 ± 0.14	3.9 ± 2.3	92.0 ± 81.5	0.82 ± 0.06	0.10 ± 0.06	Irregular
31370	53.089858	-27.781079	0.51 ± 0.26	(...)	H α	7.50 ± 0.17	1.8 ± 1.6	100.4 ± 131.7	1.42 ± 0.07	0.09 ± 0.08	Unclassifiable
11513	53.074157	-27.804923	5.61 ± 2.81	(...)	$z > 2.5$	8.92 ± 0.14	2.4 ± 1.7	(...)	(...)	(...)	Irregular
14122	53.115761	-27.786059	1.65 ± 0.83	(...)	[O III]	8.50 ± 0.08	3.3 ± 1.6	(...)	(...)	(...)	Irregular
15650	53.115894	-27.776418	1.13 ± 0.57	(...)	H β	8.41 ± 0.09	13.0 ± 2.3	(...)	(...)	(...)	Compact
16483	53.160006	-27.771002	1.91 ± 0.96	1.173	H β	8.57 ± 0.12	2.4 ± 1.8	(...)	(...)	(...)	Irregular
16798	53.125143	-27.767847	1.42 ± 0.72	(...)	H β	7.72 ± 0.11	9.3 ± 1.8	(...)	(...)	(...)	Irregular
17075	53.164651	-27.766606	1.65 ± 0.83	(...)	[O III]	8.85 ± 0.07	4.8 ± 1.8	(...)	(...)	(...)	Disk
17183	53.111168	-27.765216	1.14 ± 0.58	(...)	H β	8.34 ± 0.07	12.0 ± 2.5	(...)	(...)	(...)	Irregular
17393	53.206666	-27.763450	1.08 ± 0.55	(...)	H β	8.53 ± 0.06	7.7 ± 2.0	(...)	(...)	(...)	Disk
17686	53.120235	-27.760870	1.79 ± 0.90	(...)	[O III]	8.36 ± 0.08	3.8 ± 1.0	(...)	(...)	(...)	Irregular
17704	53.115577	-27.760782	0.14 ± 0.08	(...)	[S III]	6.80 ± 0.27	1.9 ± 2.0	(...)	(...)	(...)	Irregular
18444	53.109247	-27.754127	2.92 ± 0.13	(...)	$z > 2.5$	7.97 ± 0.09	1.7 ± 1.9	(...)	(...)	(...)	Irregular
18684	53.130594	-27.752070	1.26 ± 0.64	(...)	H β	8.62 ± 0.04	1.7 ± 1.7	(...)	(...)	(...)	Irregular
19214	53.058253	-27.748481	0.89 ± 0.45	(...)	H β	9.39 ± 0.07	3.2 ± 2.4	(...)	(...)	(...)	Irregular
34118	53.132941	-27.679610	1.35 ± 0.68	(...)	H β	7.96 ± 0.15	3.3 ± 1.6	(...)	(...)	(...)	Irregular
3148	53.179710	-27.702845	(...)	(...)	(...)	30.9 ± 2.2	(...)	(...)	(...)	(...)	Spheroidal

Table 3. continued.

ID	$\alpha(J2000)$ (deg)	$\delta(J2000)$ (deg)	z_{phot}	z_{spec}	Line	$\log(M/M_{\odot})$	f_i ($10^{-18} \text{ erg s}^{-1} \text{ cm}^{-2}$)	EW($H\alpha$) (\AA)	A($H\alpha$) (mag)	SFR _{cor} ($M_{\odot} \text{ yr}^{-1}$)	Morphology
3151	53.175771	-27.704078	(...)	(...)	(...)	(...)	6.1 ± 1.9	(...)	(...)	(...)	(...)
3361	53.150852	-27.667993	(...)	(...)	(...)	(...)	72.7 ± 2.6	(...)	(...)	(...)	(...)
3606	53.037469	-27.710118	(...)	(...)	(...)	(...)	4.5 ± 0.6	(...)	(...)	(...)	(...)

Notes. The table is separated into three parts with horizontal lines. First: $H\alpha$ emitters sample (28 galaxies; ID and coordinates from CANDELS). Second: other ELGs with CANDELS counterpart (14 galaxies; ID and coordinates from CANDELS). Third: Not-confirmed candidates from the raw sample (4 objects; ID and coordinates from our original survey; the complete original ID is HAWKI000 followed by the number in the table).

^(c) Simplified notation: [S II] λ 9069 emitters at $z \sim 0.2$ are indicated as [S II]; $H\beta$ or [O II] λ 4959,5007 at $z \sim 1.1$ as $H\beta$; [O II] λ 3727 at $z \sim 1.8$ as [O II].